Measurement of $e^+e^-\to D\bar{D}$ cross sections at the $\psi(3770)$ resonance*

M. Ablikim(麦迪娜)[1] M. N. Achasov[9,d] S. Ahmed[14] M. Albrecht[4] M. Alekseev[55A,55C] A. Amoroso[55A,55C] F. F. An(安芬芬)[1] Q. An(安琪)[42,52] Y. Bai(白羽)[41] O. Bakina[26] R. Baldini Ferroli[22A] Y. Ban(班勇)[34] K. Begzsuren[24] D. W. Bennett[21] J. V. Bennett[5] N. Berger[25] M. Bertani[22A] D. Bettoni[23A] J. M. Bian(边渐鸣)[49] F. Bianchi[55A,55C] E. Boger[26,b] I. Boyko[26] R. A. Briere[5] H. Cai(蔡浩)[57] X. Cai(蔡啸)[1,42] O. Cakir[45A] A. Calcaterra[22A] G. F. Cao(曹国富)[1,46] S. A. Cetin[45B] J. Chai[55C] J. F. Chang(常劲帆)[1,42] W. L. Chang[1,46] G. Chelkov[26,b,c] G. Chen(陈刚)[1] H. S. Chen(陈和生)[1,46] J. C. Chen(陈江川)[1] M. L. Chen(陈玛丽)[1,42] P. L. Chen(陈平亮)[53] S. J. Chen(陈申见)[32] X. R. Chen(陈旭荣)[29] Y. B. Chen(陈元柏)[1,42] X. K. Chu(褚新坤)[34] G. Cibinetto[23A] F. Cossio[55C] H. L. Dai(代洪亮)[1,42] J. P. Dai(代建平)[37,h] A. Dbeyssi[14] D. Dedovich[26] Z. Y. Deng(邓子艳)[1] A. Denig[25] I. Denysenko[26] M. Destefanis[55A,55C] F. De Mori[55A,55C] Y. Ding(丁勇)[30] C. Dong(董超)[33] J. Dong(董静)[1,42] L. Y. Dong(董燎原)[1,46] M. Y. Dong(董明义)[1] Z. L. Dou(豆正磊)[32] S. X. Du(杜书先)[60] P. F. Duan(段鹏飞)[1] J. Fang(方建)[1,42] S. S. Fang(房双世)[1,46] Y. Fang(方易)[1] R. Farinelli[23A,23B] L. Fava[55B,55C] S. Fegan[25] F. Feldbauer[4] G. Felici[22A] C. Q. Feng(封常青)[42,52] E. Fioravanti[23A] M. Fritsch[4] C. D. Fu(傅成栋)[1] Q. Gao(高清)[1] X. L. Gao(高鑫磊)[42,52] Y. Gao(高原宁)[44] Y. G. Gao(高勇贵)[6] Z. Gao(高榛)[42,52] B. Garillon[25] I. Garzia[23A] A. Gilman[49] K. Goetzen[10] L. Gong(龚丽)[33] W. X. Gong(龚文煊)[1,42] W. Gradl[25] M. Greco[55A,55C] L. M. Gu(谷立民)[32] M. H. Gu(顾旻皓)[1,42] Y. T. Gu(顾运厅)[12] A. Q. Guo(郭爱强)[1] L. B. Guo(郭立波)[31] R. P. Guo(郭如盼)[1,46] Y. P. Guo(郭玉萍)[25] A. Guskov[26] Z. Haddadi[28] S. Han(韩爽)[57] X. Q. Hao(郝喜庆)[15] F. A. Harris[47] K. L. He(何康林)[1,46] X. Q. He(何希勤)[51] F. H. Heinsius[4] T. Held[4] Y. K. Heng(衡月昆)[1] T. Holtmann[4] Z. L. Hou(侯治龙)[1] H. M. Hu(胡海明)[1,46] J. F. Hu(胡继峰)[37,h] T. Hu(胡涛)[1] Y. Hu(胡誉)[1] G. S. Huang(黄光顺)[42,52] J. S. Huang(黄金书)[15] X. T. Huang(黄性涛)[36] X. Z. Huang(黄晓忠)[32] Z. L. Huang(黄智玲)[30] T. Hussain[54] W. Ikegami Andersson[56] M, Irshad[42,52] Q. Ji(纪全)[1] Q. P. Ji(姬清平)[15] X. B. Ji(季晓斌)[1,46] X. L. Ji(季筱璐)[1,42] X. S. Jiang(江晓山)[1] X. Y. Jiang(蒋兴雨)[33] J. B. Jiao(焦健斌)[36] Z. Jiao(焦铮)[17] D. P. Jin(金大鹏)[1] S. Jin(金山)[1,46] Y. Jin(金毅)[48] T. Johansson[56] A. Julin[49] N. Kalantar-Nayestanaki[28] X. S. Kang(康晓珅)[33] M. Kavatsyuk[28] B. C. Ke(柯百谦)[1] T. Khan[42,52] A. Khoukaz[50] P. Kiese[25] R. Kliemt[10] L. Koch[27] O. B. Kolcu[45B,f] B. Kopf[4] M. Kornicer[47] M. Kuemmel[4] M. Kuessner[4] A. Kupsc[56] M. Kurth[1] W. Kühn[27] J. S. Lange[27] M. Lara[21] P. Larin[14] L. Lavezzi[55C,1] S. Leiber[4] H. Leithoff[25] C. Li(李翠)[56] Cheng Li(李澄)[42,52] D. M. Li(李德民)[60] F. Li(李飞)[1,42] F. Y. Li(李峰云)[34] G. Li(李刚)[1] H. B. Li(李海波)[1,46] H. J. Li(李惠静)[1,46] J. C. Li(李家才)[1] J. W. Li(李井文)[40] K. J. Li(李凯杰)[43] Kang Li(李康)[13] Ke Li(李科)[1] Lei Li(李蕾)[3] P. L. Li(李佩莲)[42,52] P. R. Li(李培荣)[7,46] Q. Y. Li(李启云)[36] T. Li(李腾)[36] W. D. Li(李卫东)[1,46] W. G. Li(李卫国)[1] X. L. Li(李晓玲)[36] X. N. Li(李小男)[1,42] X. Q. Li(李学潜)[33] Z. B. Li(李志兵)[43] H. Liang(梁昊)[42,52] Y. F. Liang(梁勇飞)[39] Y. T. Liang(梁羽铁)[27] G. R. Liao(廖广睿)[11] L. Z. Liao(廖龙洲)[1,46] J. Libby[20] C. X. Lin(林创新)[43] D. X. Lin(林德旭)[14] B. Liu(刘冰)[37,h] B. J. Liu(刘北江)[1] C. X. Liu(刘春秀)[1] D. Liu(刘栋)[42,52] D. Y. Liu(刘殿宇)[37,h] F. H. Liu(刘福虎)[38] Fang Liu(刘芳)[1] Feng Liu(刘峰)[6] H. B. Liu(刘宏邦)[12] H. L Liu(刘恒君)[41] H. M. Liu(刘怀民)[1,46] Huanhuan Liu(刘欢欢)[1] Huihui Liu(刘汇慧)[16] J. B. Liu(刘建北)[42,52] J. Y. Liu(刘晶译)[1,46] K. Liu(刘凯)[44] K. Y. Liu(刘魁勇)[30] Ke Liu(刘珂)[6] L. D. Liu(刘兰雕)[34] Q. Liu(刘倩)[46] S. B. Liu(刘树彬)[42,52] X. Liu(刘翔)[29] Y. B. Liu(刘玉斌)[33] Z. A. Liu(刘振安)[1] Zhiqing Liu(刘智青)[25] Y. F. Long(龙云飞)[34] X. C. Lou(娄辛丑)[1] H. J. Lu(吕海江)[17] J. G. Lu(吕军光)[1,42] Y. Lu(卢宇)[1] Y. P. Lu(卢云鹏)[1,42] C. L. Luo(罗成林)[31] M. X. Luo(罗民兴)[59] X. L. Luo(罗小兰)[1,42] S. Lusso[55C] X. R. Lyu(吕晓睿)[46] F. C. Ma(马凤才)[30] H. L. Ma(马海龙)[1] L. L. Ma(马连良)[36] M. M. Ma(马明明)[1,46] Q. M. Ma(马秋梅)[1] X. N. Ma(马旭宁)[33] X. Y. Ma(马骁妍)[1,42] Y. M. Ma(马玉明)[36] F. E. Maas[14] M. Maggiora[55A,55C] Q. A. Malik[54] A. Mangoni[22B] Y. J. Mao(冒亚军)[34] Z. P. Mao(毛泽普)[1] S. Marcello[55A,55C] Z. X. Meng(孟召霞)[48] J. G. Messchendorp[28] G. Mezzadri[23A] J. Min(闵建)[1,42] T. J. Min(闵天觉)[1] R. E. Mitchell[21] X. H. Mo(莫晓虎)[1] Y. J. Mo(莫玉俊)[6] C. Morales Morales[14] G. Morello[22A] N. Yu. Muchnoi[9,d] H. Muramatsu(村松創)[49] A. Mustafa[4] S. Nakhoul[10,g] Y. Nefedov[26] F. Nerling[10] I. B. Nikolaev[9,d] Z. Ning(宁哲)[1,42] S. Nisar[8] S. L. Niu(牛顺利)[1,42] X. Y. Niu(牛讯伊)[1,46] S. L. Olsen(馬鵬)[35,j] Q. Ouyang(欧阳群)[1] S. Pacetti[22B] Y. Pan(潘越)[42,52] M. Papenbrock[56] P. Patteri[22A] M. Pelizaeus[4] J. Pellegrino[55A,55C] H. P. Peng(彭海平)[42,52] Z. Y. Peng(彭志远)[12] K. Peters[10,g] J. Pettersson[56] J. L. Ping(平加伦)[31] R. G. Ping(平荣刚)[1,46] A. Pitka[4] R. Poling[49] V. Prasad[42,52] H. R. Qi(漆红

Received 17 March 2018, Published online 20 June 2018

∗ Supported by National Key Basic Research Program of China (2015CB856700), National Natural Science Foundation of China (NSFC) (11235011, 11335008, 11425524, 11625523, 11635010), the Chinese Academy of Sciences (CAS) Large-Scale Scientific Facility Program, the CAS Center for Excellence in Particle Physics (CCEPP), Joint Large-Scale Scientific Facility Funds of the NSFC and CAS (U1332201, U1532257, U1532258), CAS Key Research Program of Frontier Sciences (QYZDJ-SSW-SLH003, QYZDJ-SSW-SLH040), 100 Talents Program of CAS, National 1000 Talents Program of China, INPAC and Shanghai Key Laboratory for Particle Physics and Cosmology, German Research Foundation DFG under Contracts Nos. Collaborative Research Center CRC 1044, FOR 2359, Istituto Nazionale di Fisica Nucleare, Italy, Koninklijke Nederlandse Akademie van Wetenschappen (KNAW) (530-4CDP03), Ministry of Development of Turkey (DPT2006K-120470), National Science and Technology fund, The Swedish Research Council, U. S. Department of Energy (DE-FG02-05ER41374, DE-SC-0010118, DE-SC-0010504, DE-SC-0012069), University of Groningen (RuG) and the Helmholtzzentrum fuer Schwerionenforschung GmbH (GSI), Darmstadt, WCU Program of National Research Foundation of Korea (R32-2008-000-10155-0)

荣)[2] M. Qi(祁鸣)[32] T. Y. Qi(齐天钰)[2] S. Qian(钱森)[1,42] C. F. Qiao(乔从丰)[46] N. Qin(覃拈)[57] X. S. Qin[4] Z. H. Qin(秦中华)[1,42] J. F. Qiu(邱进发)[1] K. H. Rashid[54,i] C. F. Redmer[25] M. Richter[4] M. Ripka[25] M. Rolo[55C] G. Rong(荣刚)[1,46] Ch. Rosner[14] X. D. Ruan(阮向东)[12] A. Sarantsev[26,e] M. Savrié[23B] C. Schnier[4] K. Schoenning[56] W. Shan(单葳)[18] X. Y. Shan(单心钰)[42,52] M. Shao(邵明)[42,52] C. P. Shen(沈成平)[2] P. X. Shen(沈培迅)[33] X. Y. Shen(沈肖雁)[1,46] H. Y. Sheng(盛华义)[1] X. Shi(史欣)[1,42] J. J. Song(宋娇娇)[36] W. M. Song[36] X. Y. Song(宋欣颖)[1] S. Sosio[55A,55C] C. Sowa[4] S. Spataro[55A,55C] G. X. Sun(孙功星)[1] J. F. Sun(孙俊峰)[15] L. Sun(孙亮)[57] S. S. Sun(孙胜森)[1,46] X. H. Sun(孙新华)[1] Y. J. Sun(孙勇杰)[42,52] Y. K Sun(孙艳坤)[42,52] Y. Z. Sun(孙永昭)[1] Z. J. Sun(孙志嘉)[1,42] Z. T. Sun(孙振田)[21] Y. T Tan(谭雅星)[42,52] C. J. Tang(唐昌建)[39] G. Y. Tang(唐光毅)[1] X. Tang(唐晓)[1] I. Tapan[45C] M. Tiemens[28] D. Toth[49] B. Tsednee[24] I. Uman[45D] G. S. Varner[47] B. Wang(王斌)[1] B. L. Wang(王滨龙)[46] C. W. Wang(王成伟)[32] D. Wang(王东)[34] D. Y. Wang(王大勇)[34] Dan Wang(王丹)[46] K. Wang(王科)[1,42] L. L. Wang(王亮亮)[1] L. S. Wang(王灵淑)[1] M. Wang(王萌)[36] Meng Wang(王蒙)[1,46] P. Wang(王平)[1] P. L. Wang(王佩良)[1] W. P. Wang(王维平)[42,52] X. F. Wang(王雄飞)[1] Y. Wang(王越)[42,52] Y. F. Wang(王贻芳)[1] Y. Q. Wang(王亚乾)[25] Z. Wang(王铮)[1,42] Z. G. Wang(王志刚)[1,42] Z. Y. Wang(王至勇)[1] Zongyuan Wang(王宗源)[1,46] T. Weber[4] D. H. Wei(魏代会)[11] P. Weidenkaff[25] S. P. Wen(文硕频)[1] U. Wiedner[4] M. Wolke[56] L. H. Wu(伍灵慧)[1] L. J. Wu(吴连近)[1,46] Z. Wu(吴智)[1,42] L. Xia(夏磊)[42,52] X. Xia[36] Y. Xia(夏宇)[19] D. Xiao(肖栋)[1] Y. J. Xiao(肖言佳)[1,46] Z. J. Xiao(肖振军)[31] Y. G. Xie(谢宇广)[1,42] Y. H. Xie(谢跃红)[6] X. A. Xiong(熊习安)[1,46] Q. L. Xiu(修青磊)[1,42] G. F. Xu(许国发)[1] J. J. Xu(徐静静)[1,46] L. Xu(徐雷)[1] Q. J. Xu(徐庆君)[13] Q. N. Xu(徐庆年)[46] X. P. Xu(徐新平)[40] F. Yan(严芳)[53] L. Yan(严亮)[55A,55C] W. B. Yan(鄢文标)[42,52] W. C. Yan(闫文成)[2] Y. H. Yan(颜永红)[19] H. J. Yang(杨海军)[37,h] H. X. Yang(杨洪勋)[1] L. Yang(杨柳)[57] S. L. Yang(杨双莉)[1,46] Y. H. Yang(杨友华)[32] Y. X. Yang(杨永栩)[11] Yifan Yang(杨翊凡)[1,46] M. Ye(叶梅)[1,42] M. H. Ye(叶铭汉)[7] J. H. Yin(殷俊昊)[1] Z. Y. You(尤郑昀)[43] B. X. Yu(俞伯祥)[1] C. X. Yu(喻纯旭)[33] J. S. Yu(俞洁晟)[29] C. Z. Yuan(苑长征)[1,46] Y. Yuan(袁野)[1] A. Yuncu[45B,a] A. A. Zafar[54] A. Zallo[22A] Y. Zeng(曾云)[19] Z. Zeng(曾哲)[42,52] B. X. Zhang(张丙新)[1] B. Y. Zhang(张炳云)[1,42] C. C. Zhang(张长春)[1] D. H. Zhang(张达华)[1] H. H. Zhang(张宏浩)[43] H. Y. Zhang(章红宇)[1,42] J. Zhang(张晋)[1,46] J. L. Zhang(张杰磊)[58] J. Q. Zhang[4] J. W. Zhang(张家文)[1] J. Y. Zhang(张建勇)[1] J. Z. Zhang(张景芝)[1,46] K. Zhang(张坤)[1,46] L. Zhang(张磊)[44] S. F. Zhang(张思凡)[32] T. J. Zhang(张天骄)[37,h] X. Y. Zhang(张学尧)[36] Y. Zhang(张言)[42,52] Y. H. Zhang(张银鸿)[1,42] Y. T. Zhang(张亚腾)[42,52] Yang Zhang(张洋)[1] Yao Zhang(张瑶)[1] Yu Zhang(张宇)[46] Z. H. Zhang(张正好)[6] Z. P. Zhang(张子平)[52] Z. Y. Zhang(张振宇)[57] G. Zhao(赵光)[1] J. W. Zhao(赵京伟)[1,42] J. Y. Zhao(赵静宜)[1,46] J. Z. Zhao(赵京周)[1,42] Lei Zhao(赵雷)[42,52] Ling Zhao(赵玲)[1] M. G. Zhao(赵明刚)[33] Q. Zhao(赵强)[1] S. J. Zhao(赵书俊)[60] T. C. Zhao(赵天池)[1] Y. B. Zhao(赵豫斌)[1,42] Z. G. Zhao(赵政国)[42,52] A. Zhemchugov[26,b] B. Zheng(郑波)[53] J. P. Zheng(郑建平)[1,42] W. J. Zheng(郑文静)[36] Y. H. Zheng(郑阳恒)[46] B. Zhong(钟彬)[31] L. Zhou(周莉)[1,42] Q. Zhou(周巧)[1,46] X. Zhou(周详)[57] X. K. Zhou(周晓康)[42,52] X. R. Zhou(周小蓉)[42,52] X. Y. Zhou(周兴玉)[1] A. N. Zhu(朱傲男)[1,46] J. Zhu(朱江)[33] J. Zhu(朱江)[43] K. Zhu(朱凯)[1] K. J. Zhu(朱科军)[1] S. Zhu(朱帅)[1] S. H. Zhu(朱世海)[51] X. L. Zhu(朱相雷)[44] Y. C. Zhu(朱莹春)[42,52] Y. S. Zhu(朱永生)[1,46] Z. A. Zhu(朱自安)[1,46] J. Zhuang(庄建)[1,42] B. S. Zou(邹冰松)[1] J. H. Zou(邹佳恒)[1]

(BESIII Collaboration)

[1] Institute of High Energy Physics, Beijing 100049, China
[2] Beihang University, Beijing 100191, China
[3] Beijing Institute of Petrochemical Technology, Beijing 102617, China
[4] Bochum Ruhr-University, D-44780 Bochum, Germany
[5] Carnegie Mellon University, Pittsburgh, Pennsylvania 15213, USA
[6] Central China Normal University, Wuhan 430079, China
[7] China Center of Advanced Science and Technology, Beijing 100190, China
[8] COMSATS Institute of Information Technology, Lahore, Defence Road, Off Raiwind Road, 54000 Lahore, Pakistan
[9] G.I. Budker Institute of Nuclear Physics SB RAS (BINP), Novosibirsk 630090, Russia
[10] GSI Helmholtzcentre for Heavy Ion Research GmbH, D-64291 Darmstadt, Germany
[11] Guangxi Normal University, Guilin 541004, China
[12] Guangxi University, Nanning 530004, China
[13] Hangzhou Normal University, Hangzhou 310036, China
[14] Helmholtz Institute Mainz, Johann-Joachim-Becher-Weg 45, D-55099 Mainz, Germany
[15] Henan Normal University, Xinxiang 453007, China
[16] Henan University of Science and Technology, Luoyang 471003, China
[17] Huangshan College, Huangshan 245000, China
[18] Hunan Normal University, Changsha 410081, China
[19] Hunan University, Changsha 410082, China
[20] Indian Institute of Technology Madras, Chennai 600036, India
[21] Indiana University, Bloomington, Indiana 47405, USA
[22] (A)INFN Laboratori Nazionali di Frascati, I-00044, Frascati, Italy; (B)INFN and University of Perugia, I-06100, Perugia, Italy
[23] (A)INFN Sezione di Ferrara, I-44122, Ferrara, Italy; (B)University of Ferrara, I-44122, Ferrara, Italy
[24] Institute of Physics and Technology, Peace Ave. 54B, Ulaanbaatar 13330, Mongolia
[25] Johannes Gutenberg University of Mainz, Johann-Joachim-Becher-Weg 45, D-55099 Mainz, Germany
[26] Joint Institute for Nuclear Research, 141980 Dubna, Moscow region, Russia
[27] Justus-Liebig-Universitaet Giessen, II. Physikalisches Institut, Heinrich-Buff-Ring 16, D-35392 Giessen, Germany
[28] KVI-CART, University of Groningen, NL-9747 AA Groningen, The Netherlands
[29] Lanzhou University, Lanzhou 730000, China
[30] Liaoning University, Shenyang 110036, China
[31] Nanjing Normal University, Nanjing 210023, China

[32] Nanjing University, Nanjing 210093, China
[33] Nankai University, Tianjin 300071, China
[34] Peking University, Beijing 100871, China
[35] Seoul National University, Seoul, 151-747, Korea
[36] Shandong University, Jinan 250100, China
[37] Shanghai Jiao Tong University, Shanghai 200240, China
[38] Shanxi University, Taiyuan 030006, China
[39] Sichuan University, Chengdu 610064, China
[40] Soochow University, Suzhou 215006, China
[41] Southeast University, Nanjing 211100, China
[42] State Key Laboratory of Particle Detection and Electronics, Beijing 100049, Hefei 230026, China
[43] Sun Yat-Sen University, Guangzhou 510275, China
[44] Tsinghua University, Beijing 100084, China
[45] (A)Ankara University, 06100 Tandogan, Ankara, Turkey; (B)Istanbul Bilgi University, 34060 Eyup, Istanbul, Turkey; (C)Uludag University, 16059 Bursa, Turkey; (D)Near East University, Nicosia, North Cyprus, Mersin 10, Turkey
[46] University of Chinese Academy of Sciences, Beijing 100049, China
[47] University of Hawaii, Honolulu, Hawaii 96822, USA
[48] University of Jinan, Jinan 250022, China
[49] University of Minnesota, Minneapolis, Minnesota 55455, USA
[50] University of Muenster, Wilhelm-Klemm-Str. 9, 48149 Muenster, Germany
[51] University of Science and Technology Liaoning, Anshan 114051, China
[52] University of Science and Technology of China, Hefei 230026, China
[53] University of South China, Hengyang 421001, China
[54] University of the Punjab, Lahore-54590, Pakistan
[55] (A)University of Turin, I-10125, Turin, Italy; (B)University of Eastern Piedmont, I-15121, Alessandria, Italy; (C)INFN, I-10125, Turin, Italy
[56] Uppsala University, Box 516, SE-75120 Uppsala, Sweden
[57] Wuhan University, Wuhan 430072, China
[58] Xinyang Normal University, Xinyang 464000, China
[59] Zhejiang University, Hangzhou 310027, China
[60] Zhengzhou University, Zhengzhou 450001, China

[a] Also at Bogazici University, 34342 Istanbul, Turkey
[b] Also at the Moscow Institute of Physics and Technology, Moscow 141700, Russia
[c] Also at the Functional Electronics Laboratory, Tomsk State University, Tomsk, 634050, Russia
[d] Also at the Novosibirsk State University, Novosibirsk, 630090, Russia
[e] Also at the NRC "Kurchatov Institute", PNPI, 188300, Gatchina, Russia
[f] Also at Istanbul Arel University, 34295 Istanbul, Turkey
[g] Also at Goethe University Frankfurt, 60323 Frankfurt am Main, Germany
[h] Also at Key Laboratory for Particle Physics, Astrophysics and Cosmology, Ministry of Education; Shanghai Key Laboratory for Particle Physics and Cosmology; Institute of Nuclear and Particle Physics, Shanghai 200240, China
[i] Also at Government College Women University, Sialkot - 51310. Punjab, Pakistan.
[j] Currently at: Center for Underground Physics, Institute for Basic Science, Daejeon 34126, Korea

Abstract: We report new measurements of the cross sections for the production of $D\bar{D}$ final states at the $\psi(3770)$ resonance. Our data sample consists of an integrated luminosity of 2.93 fb^{-1} of e^+e^- annihilation data produced by the BEPCII collider and collected and analyzed with the BESIII detector. We exclusively reconstruct three D^0 and six D^+ hadronic decay modes and use the ratio of the yield of fully reconstructed $D\bar{D}$ events ("double tags") to the yield of all reconstructed D or $\bar{D}$ mesons ("single tags") to determine the number of $D^0\bar{D}^0$ and D^+D^- events, benefiting from the cancellation of many systematic uncertainties. Combining these yields with an independent determination of the integrated luminosity of the data sample, we find the cross sections to be $\sigma(e^+e^-\to D^0\bar{D}^0)=(3.615\pm0.010\pm0.038)$ nb and $\sigma(e^+e^-\to D^+D^-)=(2.830\pm0.011\pm0.026)$ nb, where the uncertainties are statistical and systematic, respectively.

Keywords: charm mesons, cross sections, BESIII/BEPCII

PACS: 13.25.Ft, 13.25.Gv, 13.66.Bc **DOI:** 10.1088/1674-1137/42/8/083001

1 Introduction

The $\psi(3770)$ resonance is the lowest-energy charmonium state above the threshold for decay to charmed meson pairs. The expectation that the $\psi(3770)$ should decay predominantly to $D^0\bar{D}^0$ and D^+D^- has been validated by experiment [1], although inconsistent results for the branching fraction of $\psi(3770)$ to non-$D\bar{D}$ final states have been reported [2, 3]. The cross sections $\sigma(e^+e^-\to D^0\bar{D}^0)$ and $\sigma(e^+e^-\to D^+D^-)$ at center-of-mass energy $E_{\rm cm}$ =3.773 GeV, the peak of the $\psi(3770)$ resonance, can be measured precisely and are necessary input for normalizing some measurements of charmed meson properties in $\psi(3770)$ decays. The most precise

determinations to date are from the CLEO-c Collaboration [4] using 818 pb^{-1} of e^+e^- annihilation data at $E_{\rm cm}$= 3774±1 MeV, $\sigma(e^+e^-\to D^0\bar{D}^0)$=(3.607±0.017±0.056) nb and $\sigma(e^+e^-\to D^+D^-)$ = (2.882±0.018±0.042) nb. In this paper we report measurements of the D$\bar{\rm D}$ cross sections using fully reconstructed D^0 and D^+ mesons in a ψ(3770) data sample that is approximately 3.6 times larger than CLEO-c's. Here and throughout this paper, charge-conjugate modes are implied unless explicitly stated.

Our procedure is an application of the D-tagging technique developed by the MARK III Collaboration [5], exploiting the kinematics of D$\bar{\rm D}$ production just above threshold at the ψ(3770) resonance. We use ratios of fully reconstructed D mesons ("single tags") and D$\bar{\rm D}$ events ("double tags") to determine the total numbers of D$\bar{\rm D}$ pairs. This procedure benefits from the cancellation of systematic uncertainties associated with efficiencies and input branching fractions, giving better overall precision than measurements based on single tags. The production of $D^0\bar{D}^0$ pairs in a pure $C=-1$ state complicates the interpretation of measurements at ψ(3770) by introducing correlations between the D^0 and $\bar{D}^0$ decays. We apply corrections derived by Asner and Sun [6] to remove the bias introduced by these correlations.

2 BESIII detector

Our measurement has been made with the BESIII detector at the BEPCII collider of the Institute for High Energy Physics in Beijing. Data were collected at the ψ(3770) peak, with $E_{\rm cm} = 3.773$ GeV. The integrated luminosity of this sample has previously been determined with large-angle Bhabha scattering events to be 2.93 fb^{-1} [7, 8], with an uncertainty of 0.5% dominated by systematic effects. An additional data sample of 44.9 pb^{-1} at $E_{\rm cm} = 3.650$ GeV has been used to assess potential background from continuum production under the ψ(3770).

BESIII is a general-purpose magnetic spectrometer with a geometrical acceptance of 93% of 4π. Charged particles are reconstructed in a 43-layer helium-gas-based drift chamber (MDC), which has an average single-wire resolution of 135 μm. A uniform axial magnetic field of 1 T is provided by a superconducting solenoid, allowing the precise measurement of charged particle trajectories. The resolution varies as a function of momentum, and is 0.5% at 1.0 GeV/c. The MDC is also instrumented to measure the specific ionization (dE/dx) of charged particles for particle identification. Additional particle identification is provided by a time-of-flight system (TOF) constructed as a cylindrical ("barrel") structure with two 5-cm-thick plastic-scintillator layers and two "end caps" with one 5-cm layer. The time resolution in the barrel is approximately 80 ps, and in the end caps it is 110 ps. Just beyond the TOF is an electromagnetic calorimeter (EMC) consisting of 6240 CsI(Tl) crystals, also configured as a barrel and two end caps. For 1.0-GeV photons, the energy resolution is 2.5% in the barrel and it is 5% in the end caps. This entire inner detector resides in the solenoidal magnet, which is supported by an octagonal flux-return yoke instrumented with resistive-plate counters interleaved with steel for muon identification (MUC). More detailed information on the design and performance of the BESIII detector can be found in Ref. [9].

3 Technique

To select a D$\bar{\rm D}$ event, we fully reconstruct a D using tag modes that have sizable branching fractions and can be reconstructed with good efficiency and reasonable background. We use three D^0 and six D^+ tag modes: $D^0\to K^-\pi^+$, $D^0\to K^-\pi^+\pi^0$, $D^0\to K^-\pi^+\pi^+\pi^-$, $D^+\to K^-\pi^+\pi^+$, $D^+\to K^-\pi^+\pi^+\pi^0$, $D^+\to K^0_S\pi^+$, $D^+\to K^0_S\pi^+\pi^0$, $D^+\to K^0_S\pi^+\pi^+\pi^-$, and $D^+\to K^-K^+\pi^+$.

When both the D and $\bar{\rm D}$ in an event decay to tag modes we can fully reconstruct the entire event. These double-tag events are selected when the event has two single tags and satisfies the additional requirements that the reconstructed single tags have opposite net charge, opposite-charm D parents and no shared tracks. The yield X_i for single-tag mode i is given by Eq. (1):

$$X_i = N_{\rm D\bar{D}}\cdot\mathcal{B}(D\to i)\cdot\epsilon_i, \tag{1}$$

where $N_{\rm D\bar{D}}$ is the total number of D$\bar{\rm D}$ events, $\mathcal{B}(D\to i)$ is the branching fraction for decay mode i, and ϵ_i is the reconstruction efficiency for the mode, determined with Monte Carlo (MC) simulation. Extending this reasoning, the yields for $\bar{\rm D}$ decaying to mode j and for ij double-tag events, in which the D decays to mode i and the $\bar{\rm D}$ decays to mode j, are given as follows:

$$Y_j = N_{\rm D\bar{D}}\cdot\mathcal{B}(\bar{D}\to j)\cdot\epsilon_j, \tag{2}$$

and

$$Z_{ij} = N_{\rm D\bar{D}}\cdot\mathcal{B}(D\to i)\cdot\mathcal{B}(\bar{D}\to j)\cdot\epsilon_{ij}. \tag{3}$$

In these equations, Z_{ij} is the yield for the double-tag mode ij, and ϵ_{ij} is the efficiency for reconstructing both tags in the same event. Combining Eqs. (1), (2) and (3), $N_{\rm D\bar{D}}$ can be expressed as

$$N_{\rm D\bar{D}} = \frac{X_i\cdot Y_j\cdot\epsilon_{ij}}{Z_{ij}\cdot\epsilon_i\cdot\epsilon_j}. \tag{4}$$

The cancellation of systematic uncertainties occurs through the ratio of efficiencies $\epsilon_{ij}/(\epsilon_i\cdot\epsilon_j)$. The measured $N_{\rm D\bar{D}}$ from each combinations of i and j are then averaged, weighted by their statistical uncertainties. Finally, to determine cross sections we divide $N_{\rm D\bar{D}}$ by the inte-

grated luminosity $\mathcal{L}$ of the $\psi(3770)$ sample, $\sigma(e^+e^- \to D\bar{D}) = N_{D\bar{D}}/\mathcal{L}$.

4 Particle reconstruction

Detection efficiencies and backgrounds for this analysis have been studied with detailed simulations of the BESIII detector based on GEANT4 [10]. High-statistics MC samples were produced for generic $D^0\bar{D}^0$ and D^+D^- decays from $\psi(3770)$, $q\bar{q} \to$ light hadrons (q = u,d or s), $\tau^+\tau^-$, and radiative return to J/ψ and $\psi(3686)$. The $D^0\bar{D}^0$, D^+D^-, $q\bar{q}$, and $\tau^+\tau^-$ states were generated using KKMC [11, 12], while the $\gamma J/\psi$ and $\gamma\psi(3686)$ were generated with EvtGen [13]. All were then decayed with EvtGen, except for the $q\bar{q}$ and $\tau^+\tau^-$, which were modeled with the LUNDCHARM [14] and the TAUOLA [11, 15] generators, respectively.

Data and MC samples are treated identically for the selection of D tags. All particles used to reconstruct a candidate must pass requirements specific to the particle type. Charged particles are required to be within the fiducial region for reliable tracking ($|\cos\theta| < 0.93$, where θ is the polar angle relative to the beam direction) and to pass within 1 cm (10 cm) of the interaction point in the plane transverse to the beam direction (along the beam direction). Particle identification is based on TOF and dE/dx measurements, with the identity as a pion or kaon assigned based on which hypothesis has the higher probability. To be selected as a photon, an EMC shower must not be associated with any charged track [16], must have an EMC hit time between 0 and 700 ns to suppress activity that is not consistent with originating from the collision event, must have an energy of at least 25 MeV if it is in the barrel region of the detector ($|\cos\theta| < 0.8$), and 50 MeV if it is in the end cap region ($0.84 < |\cos\theta| < 0.92$) to suppress noise in the EMC as a potential background to real photons. Showers in the transition region between the barrel and end cap are excluded.

K^0_S mesons are reconstructed from the decay into $\pi^+\pi^-$. Because of the cleanliness of the selection and the possibility of a measurably displaced decay vertex, the pions are not required to pass the usual particle identification or interaction-point requirements. A fit is performed with the pions constrained to a common vertex and the K^0_S candidate is accepted if the fit satisfies $\chi^2 < 100$ and the candidate mass is within $\sim 3\sigma$ of the nominal K^0_S mass (487–511 MeV/c^2). The momentum of the K^0_S that is obtained from the constrained-vertex fit is used for the subsequent reconstruction of D-tag candidates. π^0 mesons are reconstructed through the decay into two photons. Both photons for a π^0 candidate must pass the above selection criteria, and at least one of them must be in the barrel region of the detector. To be accepted a π^0 candidate must have an invariant mass between 115 MeV/c^2 and 150 MeV/c^2. The photons are then refitted with a π^0 mass constraint and the resulting π^0 momentum is used for the reconstruction of D-tag candidates.

5 Event selection

In addition to the requirements on the final-state particles, the reconstructed D-tag candidates must pass several additional requirements that ensure the measured candidate energy and momentum are close to the expected values for production via $\psi(3770) \to D\bar{D}$. The first of these requirements is $\Delta E = E_D - E_{beam} \simeq 0$, where E_D is the energy of the reconstructed D candidate and E_{beam} is the beam energy. In calculating ΔE we use the beam energy calibrated with D^0 and D^+ decays, combining groups of nearby runs to obtain sufficient statistics. Selection requirements on ΔE are determined separately for each tag mode for data and MC to account for differing resolutions. As shown in Table 1, for modes decaying into all charged tracks, the requirements are set to $\pm 3\sigma$ about the mean, while for modes with a π^0, the requirements are asymmetric about the mean, extending on the low side to -4σ to accommodate the tail from the photon energy resolution.

Figure 1 shows the data and MC overlays of the ΔE distributions by mode.

Table 1. The selected range on ΔE is $\pm 3\sigma$ about the mean, except that for modes with a π^0 an extended lower bound of -4σ is used. The resolutions and means are extracted by fitting with a double Gaussian, weighted by the two Gaussian yields, and determined separately for data and MC.

Tag mode	MC		data	
	σ/MeV	mean/MeV	σ/MeV	mean/MeV
$D^0 \to K^-\pi^+$	7.6	−0.4	9.4	−0.8
$D^0 \to K^-\pi^+\pi^0$	14.1	−7.6	15.4	−7.6
$D^0 \to K^-\pi^+\pi^+\pi^-$	8.2	−1.4	9.8	−2.0
$D^+ \to K^-\pi^+\pi^+$	7.2	−0.9	8.6	−1.2
$D^+ \to K^-\pi^+\pi^+\pi^0$	12.8	−6.9	13.7	−6.9
$D^+ \to K^0_S\pi^+$	6.7	0.4	8.4	−0.1
$D^+ \to K^0_S\pi^+\pi^0$	14.6	−7.7	16.2	−7.9
$D^+ \to K^0_S\pi^+\pi^+\pi^-$	8.2	−1.1	10.4	−1.7
$D^+ \to K^+K^-\pi^+$	6.2	−1.1	7.2	−1.5

The second variable used in selecting D tags is the beam-constrained mass $M_{BC}c^2 = \sqrt{E^2_{beam} - |\boldsymbol{p}_{tag}c|^2}$, where $\boldsymbol{p}_{tag}$ is the 3-momentum of the candidate D. We use M_{BC} rather than the invariant mass because of the excellent precision with which the beam energy is known. The requirement that M_{BC} be close to the known D mass ensures that the D tag has the expected momentum. After application of the ΔE requirement to single-tag candidates of a given mode, we construct an M_{BC} dis-

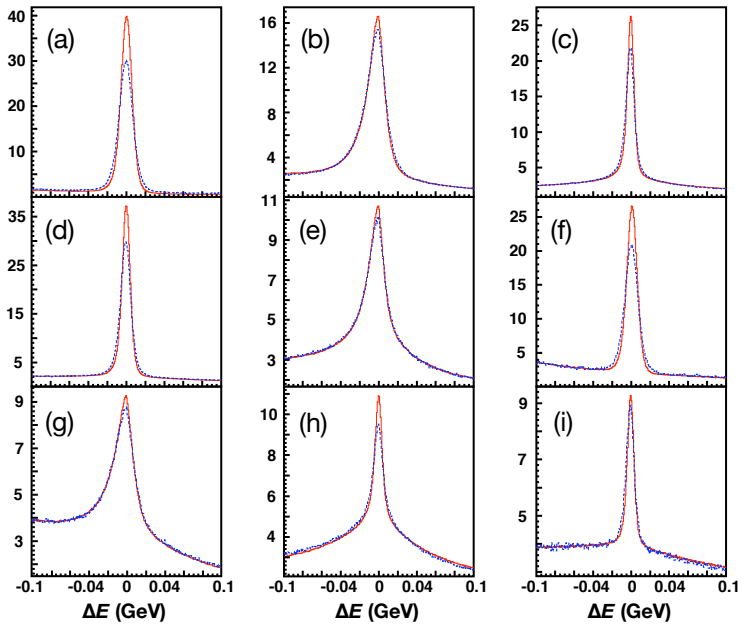

Fig. 1. (color online) ΔE line shape for various single-tag mode (arbitrarily scaled). Starting from the top left, the modes are: (a) $D^0\to K^-\pi^+$, (b) $D^0\to K^-\pi^+\pi^0$, (c) $D^0\to K^-\pi^+\pi^+\pi^-$, (d) $D^+\to K^-\pi^+\pi^+$, (e) $D^+\to K^-\pi^+\pi^+\pi^0$, (f) $D^+\to K^0_S\pi^+$, (g) $D^+\to K^0_S\pi^+\pi^0$, (h) $D^+\to K^0_S\pi^+\pi^+\pi^-$, and (i) $D^+\to K^+K^-\pi^+$. These plots overlay the 3.773 GeV data (blue dashed histograms) and the corresponding narrower-width MC (red solid histograms). Only requirements on the constituent particles and a very loose $M_{\rm BC}$ requirement ($1.83\ {\rm GeV}/c^2\leqslant M_{\rm BC}\leqslant 1.89\ {\rm GeV}/c^2$) have been applied.

tribution in the region of the known masses of charmed mesons (1.83–1.89 GeV/c^2). For the MC a small upward shift of just under 1 MeV/c is applied to the measured D momentum for the calculation of $M_{\rm BC}$ to compensate for input parameters that do not precisely match data. Initial inspection of the distribution in data for the two-body mode $D^0\to K^-\pi^+$ exhibited peaking near the high end of the $M_{\rm BC}$ range not seen in MC. We demonstrated this to be background from cosmic ray and QED events. To eliminate it from the distribution, additional requirements are applied in selecting $D^0\to K^-\pi^+$ candidates with exactly two charged tracks. We veto these events if they satisfy at least one of the following conditions: TOF information consistent with a cosmic ray event, particle identification information consistent with an e^+e^- hypothesis, two tracks with EMC energy deposits consistent with an e^+e^- hypothesis, or either track with particle identification and MUC information consistent with being a muon.

6 Yields and efficiencies

The $M_{\rm BC}$ distribution for single-tag candidates for each mode is fitted with a MC-derived signal shape and an ARGUS function background [17]. The signal shape is convolved with a double Gaussian with a common mean to allow for differences in $M_{\rm BC}$ resolution between data and MC. Charge-conjugate modes are fitted simultaneously with the double-Gaussian signal-shape parameters constrained to be the same and the normalizations and background parameters allowed to vary independently in the fit. Peaking backgrounds contributed by decay modes that have similar final states to the signal mode are included in the signal shape, although the yields are corrected after the fit to count only true signal events.

An example $M_{\rm BC}$ fit is shown in Fig. 2. (The full set of fits is provided in Appendix A.) In events with multiple single-tag candidates, the best candidate is chosen per mode and per charm to be the one with the smallest $|\Delta E|$. Based on the fit results tight mode-dependent requirements on ΔE are applied. To determine the tag yield, the $M_{\rm BC}$ histogram is integrated within the signal region, $1.8580\ {\rm GeV}/c^2\leqslant M_{\rm BC}\leqslant 1.8740\ {\rm GeV}/c^2$ for D^0 modes and $1.8628\ {\rm GeV}/c^2\leqslant M_{\rm BC}\leqslant 1.8788\ {\rm GeV}/c^2$ for D^+ modes, and then the analytic integral of the ARGUS function in this region is subtracted. The efficiency for each of the 18 single-tag modes is found by using MC truth information to determine the total number generated for the denominator and using the same cut-and-count method as used for data to determine the numerator. The single-tag yields and efficiencies are summarized in Table 2, where the efficiencies include branching fractions for $\pi^0\to\gamma\gamma$ and $K^0_S\to\pi^+\pi^-$ decays.

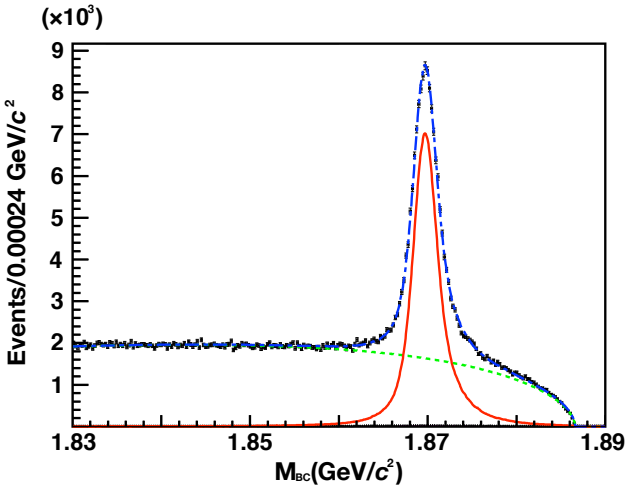

Fig. 2. (color online) $M_{\rm BC}$ fit for single-tag mode $D^+ \to K^-\pi^+\pi^+\pi^0$, from data. Blue dash-dot (green dashed) line represents the total fit (the fitted background shape) and the red solid curve corresponds to the fitted signal shape.

Table 2. Single-tag yields after subtracting their corresponding peaking backgrounds from data and efficiencies from MC, as described in the text. The uncertainties are statistical only.

tag mode	yield	efficiency(%)
$D^0\to K^-\pi^+$	260,915 ± 520	63.125 ± 0.007
$\bar{D}^0\to K^+\pi^-$	262,356 ± 522	64.272 ± 0.006
$D^0\to K^-\pi^+\pi^0$	537,923 ± 845	35.253 ± 0.007
$\bar{D}^0\to K^+\pi^-\pi^0$	544,252 ± 852	35.761 ± 0.007
$D^0\to K^-\pi^+\pi^+\pi^-$	346,583 ± 679	38.321 ± 0.007
$\bar{D}^0\to K^+\pi^+\pi^-\pi^-$	351,573 ± 687	39.082 ± 0.007
$D^+\to K^-\pi^+\pi^+$	391,786 ± 653	50.346 ± 0.005
$D^-\to K^+\pi^-\pi^-$	394,749 ± 656	51.316 ± 0.005
$D^+\to K^-\pi^+\pi^+\pi^0$	124,619 ± 529	26.138 ± 0.014
$D^-\to K^+\pi^-\pi^-\pi^0$	128,203 ± 539	26.586 ± 0.015
$D^+\to K^0_S\pi^+$	48,185 ± 229	36.726 ± 0.008
$D^-\to K^0_S\pi^-$	47,952 ± 228	36.891 ± 0.008
$D^+\to K^0_S\pi^+\pi^0$	114,919 ± 471	20.687 ± 0.011
$D^-\to K^0_S\pi^-\pi^0$	116,540 ± 472	20.690 ± 0.011
$D^+\to K^0_S\pi^+\pi^+\pi^-$	63,018 ± 421	21.966 ± 0.019
$D^-\to K^0_S\pi^+\pi^-\pi^-$	62,982 ± 421	21.988 ± 0.019
$D^+\to K^+K^-\pi^+$	34,416 ± 258	41.525 ± 0.042
$D^-\to K^+K^-\pi^-$	34,434 ± 257	41.892 ± 0.042

Double tags are fully reconstructed events in which both the D and the $\bar{\rm D}$ pass the selection criteria for one of the tag modes. In events with multiple double-tag candidates, the best candidate per mode combination per event is chosen with the $[M_{\rm BC}({\rm D})+M_{\rm BC}(\bar{\rm D})]/2$ closest to the known D mass. Following a procedure similar to the single-tag counting, we fit the two-dimensional distribution of $M_{\rm BC}(\bar{\rm D})$ vs. $M_{\rm BC}({\rm D})$ for the selected single-tag modes to define the signal region for a cut-and-count determination of the double-tag yield. A more sophisticated treatment of the background is required because of the correlations between the tags. The signal shape is again derived from MC, using truth information and including peaking backgrounds with the signal. We found that convolving the MC shape with smearing functions to account for the small data/MC resolution difference did not appreciably improve the accuracy of the tag yields, so no signal smearing is included in the double-tag fits.

The background shapes in the double-tag fits correspond to four possible ways of mis-reconstructing an event, as shown in Fig. 3. A direct product of a MC-derived signal shape with an analytic ARGUS function background, with shape parameters fixed to those of the corresponding single-tag fit, is used to represent the background contributed by events with a correctly reconstructed D and incorrectly reconstructed $\bar{\rm D}$. The background shape for the charm-conjugate case is similarly constructed. For completely reconstructed continuum events or fully reconstructed but mispartitioned $\rm D\bar{D}$ events (with particles assigned incorrectly to the D and $\bar{\rm D}$), a direct product of a double-Gaussian function and an ARGUS function rotated by 45° is used. The kinematic limit and exponent parameters of the rotated ARGUS function are fixed, while the slope parameter is allowed to be free in the fit. Finally, the remaining background events with neither D nor $\bar{\rm D}$ correctly reconstructed are modeled with a direct product of two ARGUS functions, with parameters taken from the corresponding single-tag fits. An example fit to data is shown in Fig. 4. (The full set of fits is provided in Appendix A.)

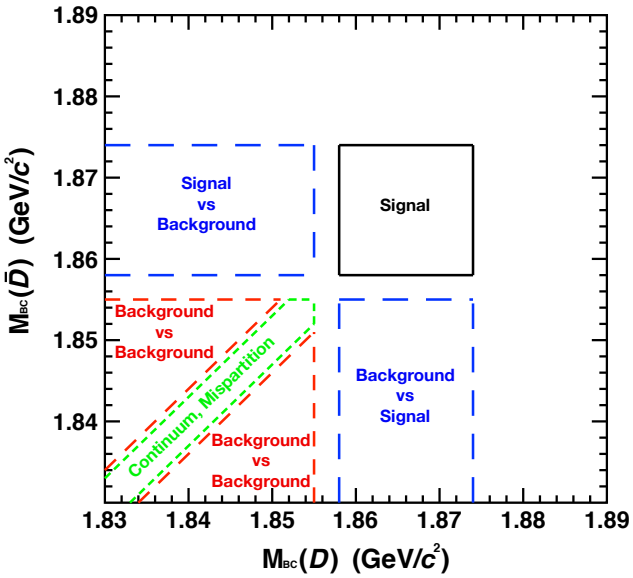

Fig. 3. (color online) The two-dimensional $M_{\rm BC}$ plane divided into regions dominated by signal and various backgrounds. These regions represent the shapes used in the double-tag fitting method and sideband corrections described in the text.

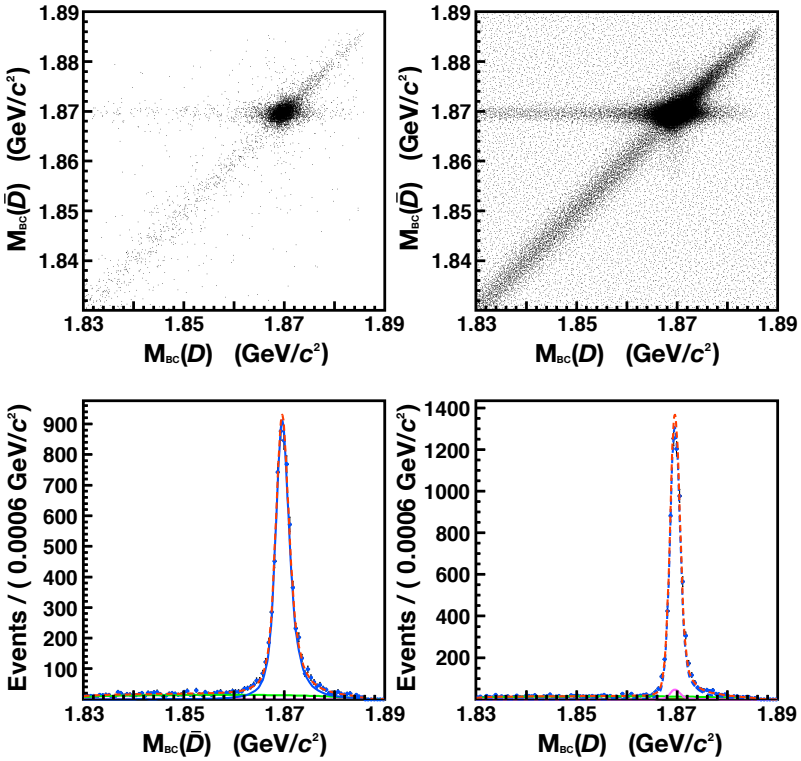

Fig. 4. (color online) Example two-dimensional $M_{\rm BC}$ double-tag fit from data as described in the text, for tag mode $K^+\pi^-\pi^-$ vs. $K^-\pi^+\pi^+\pi^0$. The top left figure is a scatter plot of the data and the top right is a scatter plot of the fit to the data. The bottom two plots are overlays of data and the fit projected onto the positive and negative charm $M_{\rm BC}$ axes. The red dashed (blue solid) lines represent the total fits (the fitted signal shapes) and the solid green curves are the fitted background shapes. The magenta curve corresponds to the case when $D^-\to K^+\pi^-\pi^-$ is reconstructed correctly, while $D^+\to K^-\pi^+\pi^+\pi^0$ is not.

After the two-dimensional fit is performed, the $M_{\rm BC}$ histogram is integrated within the same signal region as the single-tag fits, and the integrals of the four background shapes are subtracted from this total. The resultant double-tag yields and efficiencies, which include branching fractions for $\pi^0\to\gamma\gamma$ and $K^0_S\to\pi^+\pi^-$ decays, are summarized in Tables 3 and 4.

We must correct the yields determined with the $M_{\rm BC}$ fits (data and MC) for contributions from background processes that peak in the signal region. Such backgrounds come from other D decays with similar kinematics and particle compositions as the specific signal mode. We rely on MC, generated with world-average branching fractions [1], to determine the fraction of peaking background events, as well as to calculate their selection efficiencies. We apply MC-determined corrections for these in every case where more than 0.01% of the fitted yield is attributable to peaking background. The largest contribution of peaking background is for $D^+\to K^0_S\pi^+\pi^+\pi^-$, approximately 2.5% of the fitted yield. $D^0\to K^-\pi^+\pi^+\pi^-$ and $D^+\to K^0_S\pi^+\pi^0$ both have $\sim$2.0% of their fitted yields from peaking backgrounds, and all other modes have less than 1.0%. Because the peaking backgrounds come from well understood processes, like doubly Cabibbo-suppressed modes, simultaneous misidentification of both a pion and a kaon in an event, and charged pion pairs not from K^0_S decays that pass the K^0_S invariant mass requirement, we are confident that they are well modeled by the MC.

The analysis described above results in a set of measured values of $N_{\rm D\bar{D}ij}$, the number of $D\bar{D}$ events determined with the single- and double-tag yields of positive tag mode i and negative tag mode j. The uncertainties are highly mode dependent because of branching fractions, efficiencies and backgrounds, so these measurements must be combined into an uncertainty-weighted mean taking into account correlations within and between the mode-specific measurements. We use an analytic procedure for this and demonstrated its reliability with a toy MC study.

For our full 2.93 fb^{-1} $\psi(3770)$ data sample we find $N_{\rm D^0\bar{D}^0}=(10{,}621\pm29)\times10^3$ and $N_{\rm D^+D^-}=(8{,}296\pm31)\times10^3$. Using the integrated luminosity from Ref. [8], we obtain observed cross sections for $D\bar{D}$ production at the

Table 3. $D^0\bar{D}^0$ double-tag yields from data and efficiencies from MC, as described in the text. The uncertainties are statistical only.

tag mode	yield	efficiency(%)
$D^0\to K^-\pi^+$ vs. $\bar{D}^0\to K^+\pi^-$	6,545 ± 81	42.58 ± 0.13
$D^0\to K^-\pi^+$ vs. $\bar{D}^0\to K^+\pi^-\pi^0$	14,701 ± 122	24.90 ± 0.06
$D^0\to K^-\pi^+$ vs. $\bar{D}^0\to K^+\pi^+\pi^-\pi^-$	9,096 ± 96	25.54 ± 0.08
$D^0\to K^-\pi^+\pi^0$ vs. $\bar{D}^0\to K^+\pi^-$	14,526 ± 122	24.94 ± 0.06
$D^0\to K^-\pi^+\pi^0$ vs. $\bar{D}^0\to K^+\pi^-\pi^0$	30,311 ± 176	13.94 ± 0.03
$D^0\to K^-\pi^+\pi^0$ vs. $\bar{D}^0\to K^+\pi^+\pi^-\pi^-$	18,651 ± 139	14.35 ± 0.03
$D^0\to K^-\pi^+\pi^+\pi^-$ vs. $\bar{D}^0\to K^+\pi^-$	8,988 ± 96	25.77 ± 0.08
$D^0\to K^-\pi^+\pi^+\pi^-$ vs. $\bar{D}^0\to K^+\pi^-\pi^0$	18,635 ± 139	14.32 ± 0.03
$D^0\to K^-\pi^+\pi^+\pi^-$ vs. $\bar{D}^0\to K^+\pi^+\pi^-\pi^-$	11,572 ± 110	14.86 ± 0.04

Table 4. D^+D^- double-tag yields from data and efficiencies from MC, as described in the text. The uncertainties are statistical only.

tag mode	yield	efficiency(%)
$D^+\to K^-\pi^+\pi^+$ vs. $D^-\to K^+\pi^-\pi^-$	18,800 ± 138	26.02 ± 0.05
$D^+\to K^-\pi^+\pi^+$ vs. $D^-\to K^+\pi^-\pi^-\pi^0$	5,981 ± 80	13.62 ± 0.05
$D^+\to K^-\pi^+\pi^+$ vs. $D^-\to K^0_S\pi^-$	2,368 ± 49	18.45 ± 0.12
$D^+\to K^-\pi^+\pi^+$ vs. $D^-\to K^0_S\pi^-\pi^0$	5,592 ± 75	10.51 ± 0.04
$D^+\to K^-\pi^+\pi^+$ vs. $D^-\to K^0_S\pi^+\pi^-\pi^-$	2,826 ± 53	10.82 ± 0.06
$D^+\to K^-\pi^+\pi^+$ vs. $D^-\to K^+K^-\pi^-$	1,597 ± 40	20.87 ± 0.15
$D^+\to K^-\pi^+\pi^+\pi^0$ vs. $D^-\to K^+\pi^-\pi^-$	6,067 ± 80	13.48 ± 0.05
$D^+\to K^-\pi^+\pi^+\pi^0$ vs. $D^-\to K^+\pi^-\pi^-\pi^0$	1,895 ± 53	6.79 ± 0.06
$D^+\to K^-\pi^+\pi^+\pi^0$ vs. $D^-\to K^0_S\pi^-$	693 ± 26	9.82 ± 0.11
$D^+\to K^-\pi^+\pi^+\pi^0$ vs. $D^-\to K^0_S\pi^-\pi^0$	1,726 ± 44	5.22 ± 0.04
$D^+\to K^-\pi^+\pi^+\pi^0$ vs. $D^-\to K^0_S\pi^+\pi^-\pi^-$	857 ± 33	5.41 ± 0.06
$D^+\to K^-\pi^+\pi^+\pi^0$ vs. $D^-\to K^+K^-\pi^-$	549 ± 24	10.78 ± 0.15
$D^+\to K^0_S\pi^+$ vs. $D^-\to K^+\pi^-\pi^-$	2,352 ± 48	18.96 ± 0.12
$D^+\to K^0_S\pi^+$ vs. $D^-\to K^+\pi^-\pi^-\pi^0$	722 ± 27	9.80 ± 0.12
$D^+\to K^0_S\pi^+$ vs. $D^-\to K^0_S\pi^-$	269 ± 16	13.95 ± 0.27
$D^+\to K^0_S\pi^+$ vs. $D^-\to K^0_S\pi^-\pi^0$	678 ± 26	7.67 ± 0.10
$D^+\to K^0_S\pi^+$ vs. $D^-\to K^0_S\pi^+\pi^-\pi^-$	383 ± 20	7.90 ± 0.13
$D^+\to K^0_S\pi^+$ vs. $D^-\to K^+K^-\pi^-$	191 ± 14	15.2 ± 0.34
$D^+\to K^0_S\pi^+\pi^0$ vs. $D^-\to K^+\pi^-\pi^-$	5,627 ± 75	10.64 ± 0.04
$D^+\to K^0_S\pi^+\pi^0$ vs. $D^-\to K^+\pi^-\pi^-\pi^0$	1,708 ± 43	5.28 ± 0.04
$D^+\to K^0_S\pi^+\pi^0$ vs. $D^-\to K^0_S\pi^-$	624 ± 25	7.67 ± 0.10
$D^+\to K^0_S\pi^+\pi^0$ vs. $D^-\to K^0_S\pi^-\pi^0$	1,557 ± 40	4.08 ± 0.03
$D^+\to K^0_S\pi^+\pi^0$ vs. $D^-\to K^0_S\pi^+\pi^-\pi^-$	747 ± 28	4.26 ± 0.05
$D^+\to K^0_S\pi^+\pi^0$ vs. $D^-\to K^+K^-\pi^-$	503 ± 23	8.51 ± 0.13
$D^+\to K^0_S\pi^+\pi^+\pi^-$ vs. $D^-\to K^+\pi^-\pi^-$	2,857 ± 53	11.01 ± 0.06
$D^+\to K^0_S\pi^+\pi^+\pi^-$ vs. $D^-\to K^+\pi^-\pi^-\pi^0$	924 ± 34	5.44 ± 0.06
$D^+\to K^0_S\pi^+\pi^+\pi^-$ vs. $D^-\to K^0_S\pi^-$	313 ± 18	7.72 ± 0.13
$D^+\to K^0_S\pi^+\pi^+\pi^-$ vs. $D^-\to K^0_S\pi^-\pi^0$	778 ± 29	4.17 ± 0.05
$D^+\to K^0_S\pi^+\pi^+\pi^-$ vs. $D^-\to K^0_S\pi^+\pi^-\pi^-$	468 ± 24	4.28 ± 0.06
$D^+\to K^0_S\pi^+\pi^+\pi^-$ vs. $D^-\to K^+K^-\pi^-$	246 ± 18	8.96 ± 0.19
$D^+\to K^+K^-\pi^+$ vs. $D^-\to K^+\pi^-\pi^-$	1,576 ± 40	21.31 ± 0.16
$D^+\to K^+K^-\pi^+$ vs. $D^-\to K^+\pi^-\pi^-\pi^0$	509 ± 23	10.41 ± 0.15
$D^+\to K^+K^-\pi^+$ vs. $D^-\to K^0_S\pi^-$	185 ± 14	14.48 ± 0.33
$D^+\to K^+K^-\pi^+$ vs. $D^-\to K^0_S\pi^-\pi^0$	468 ± 22	8.23 ± 0.13
$D^+\to K^+K^-\pi^+$ vs. $D^-\to K^0_S\pi^+\pi^-\pi^-$	232 ± 18	8.62 ± 0.19
$D^+\to K^+K^-\pi^+$ vs. $D^-\to K^+K^-\pi^-$	156 ± 16	16.46 ± 0.53

$\psi(3770)$ of $\sigma(e^+e^- \to D^0\bar{D}^0) = (3.623\pm0.010)$ nb and $\sigma(e^+e^- \to D^+D^-) = (2.830\pm0.011)$ nb. Here, the uncertainties are statistical only. The summed χ^2 values relative to the mean for all pairs of tag modes are 13.2 for $D^0\bar{D}^0$ (9 modes) and 53.6 for D^+D^- (36 modes).

We verified the reliability of our yield measurements with an "In vs. Out" test with MC by randomly partitioning our MC (signal and background) into ten statistically independent data-sized sets. We determined single- and double-tag yields for these subsamples, calculated the $N_{D\bar{D}}$ and compared these to the true values for each. The overall χ^2 for these ten tests was 10.7 for $N_{D^0\bar{D}^0}$ and 12.4 for $N_{D^+D^-}$, demonstrating that our procedure reliably determines both $N_{D\bar{D}}$ and its statistical uncertainty. In a second test, the data sample was partitioned in time into five subsamples of approximately 0.5 fb^{-1} each and measured $\sigma(e^+e^- \to D^0\bar{D}^0)$ and $\sigma(e^+e^- \to D^+D^-)$ for each. The values of χ^2 for the hypothesis of equal values for all intervals were 5.4 and 6.0, respectively.

7 Effects of quantum correlations

As mentioned earlier in this paper, the $D^0\bar{D}^0$ yield and cross section must be corrected for correlations introduced by production through a pure $C=-1$ state at the $\psi(3770)$. Asner and Sun [6] provide correction factors that can be applied directly to our measured yields with Eq. 5 for $D^0 \to f$ and $\bar{D}^0 \to f'$ and Eq. 6 for the case $f=f'$.

$$N^{\rm measured}_{D^0\bar{D}^0} = N^{\rm true}_{D^0\bar{D}^0} \times (1 + r_f\tilde{y}_f + r_{f'}\tilde{y}_{f'} + r_f r_{f'} v^-_{ff'}) \quad (5)$$

$$N^{\rm measured}_{D^0\bar{D}^0} = N^{\rm true}_{D^0\bar{D}^0} \times (1 + 2r_f\tilde{y}_f - r_f^2(2 - z_f^2)) \quad (6)$$

The quantities appearing in these equations can be expressed in terms of measured parameters of D^0 decays and $D^0\bar{D}^0$ mixing, with $v^-_{jk} = (z_j z_k - w_j w_k)/2$, $z_j = 2\cos\delta_j$ and $w_j = 2\sin\delta_j$. r_j and δ_j are defined by $\langle j|\bar{D}^0\rangle/\langle j|D^0\rangle = r_j e^{i\delta_j}$, where $r_j = |\langle j|\bar{D}^0\rangle/\langle j|D^0\rangle|$, and δ_j is the average strong phase difference for the Cabibbo-favored tag mode. The usual mixing parameters x and y, which are related to the differences in masses and lifetimes of the two mass eigenstates, enter through $\tilde{y}_j = y\cos\delta_j + x\sin\delta_j$. The $D^0 \to K^-\pi^+\pi^0$ and $K^-\pi^+\pi^+\pi^-$ tag modes require a slightly more complicated treatment because they are mixtures of modes with different phases. This requires introducing coherence factors R_j to characterize the variation of δ_j over phase space, with z_j and w_j being redefined as $z_j = 2R_j\cos\delta_j$ and $w_j = 2R_j\sin\delta_j$ [18].

Table 5 shows the input parameters that are used to obtain the correction factors and Fig. 5 shows the corrections to $\sigma(e^+e^- \to D^0\bar{D}^0)$ for each of the nine double-tag modes, along with the average. The overall effect is a relative change in $N_{D^0\bar{D}^0}$ of approximately -0.2%, with final corrected values of $N_{D^0\bar{D}^0} = (10{,}597\pm28)\times10^3$ and $\sigma(e^+e^- \to D^0\bar{D}^0) = (3.615\pm0.010)$ nb. The uncertainties are statistical only. The summed χ^2 value relative to the mean for all pairs of tag modes is 11.8 for $D^0\bar{D}^0$ (9 modes).

Table 5. Input parameters for the quantum correlation corrections.

$x = 0.0037\pm0.0016$	[19]
$y = 0.0066^{+0.0007}_{-0.0010}$	[19]
$r^2_{K\pi} = 0.00349\pm0.00004$	[19]
$\delta_{K\pi} = (11.8^{+9.5}_{-14.7})^\circ$	[19]
$r_{K\pi\pi^0} = 0.0447\pm0.0012$	[20]
$\delta_{K\pi\pi^0} = (198^{+14}_{-15})^\circ$ (*)	[20]
$R_{K\pi\pi^0} = 0.81\pm0.06$	[20]
$r_{K3\pi} = 0.0549\pm0.0006$	[20]
$\delta_{K3\pi} = (128^{+28}_{-17})^\circ$ (*)	[20]
$R_{K3\pi} = 0.43^{+0.17}_{-0.13}$	[20]

(*) 180° difference in phase convention from Ref. [19].

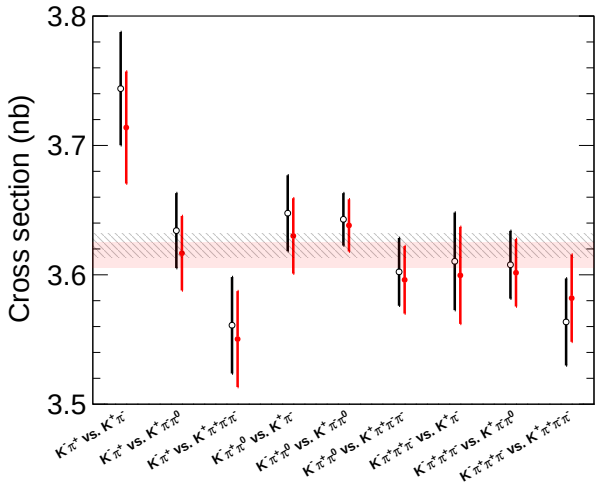

Fig. 5. (color online) $\sigma(e^+e^- \to D^0\bar{D}^0)$ for the nine double-tag modes, as labeled on the horizontal axis. The red (black) points show the $D^0\bar{D}^0$ cross section values with (without) the quantum correlation correction. The light red (black shaded) band denotes the one-standard-deviation bound of the weighted average of the corrected (uncorrected) measurements.

8 Systematic uncertainties

The sources of systematic uncertainty that have been considered for the $D^0\bar{D}^0$ and D^+D^- cross section measurements are listed in Table 6.

The double-tag technique used to determine the event yields and cross sections $\sigma(e^+e^- \to D^0\bar{D}^0)$ and $\sigma(e^+e^- \to D^+D^-)$ has the benefit of substantial cancellation of systematic uncertainties. Detector effects including tracking, particle identification, and π^0 and K^0_S reconstruction, along with tag-mode resonant substructure and the ΔE requirement, all affect both single and double tags.

There are, however, event-dependent effects that do not cancel in the efficiency ratio $\epsilon_{ij}/(\epsilon_i \cdot \epsilon_j)$. The event environment in which D mesons are tagged affects the efficiency because higher multiplicities of charged tracks or π^0s lower the tagging efficiency. This can arise due to three possible sources: (1) differences in multiplicity-dependent efficiencies between data and MC, (2) differences between the other-side multiplicities in data and MC due to imperfect knowledge of D meson decay modes and rates, and (3) sensitivity of the best candidate selection to the number of fake-tag background events.

Table 6. Systematic uncertainties in the cross section measurements in %.

source	$\sigma(e^+e^-\to D^0\bar{D}^0)$	$\sigma(e^+e^-\to D^+D^-)$
multiplicity-dependent efficiency	0.4	0.1
other-side multiplicity	<0.01	0.22
best-candidate selection	0.45	0.07
single tag fit background shape	0.54	0.64
single tag fit signal shape	0.26	0.19
double tag fit	0.28	0.19
cosmic/lepton veto	0.06	n/a
$\psi(3770)$ line shape for isr	0.15	0.25
fsr simulation	0.11	0.10
quantum correlation correction	0.2	n/a
integrated luminosity	0.5	0.5
total	1.05	0.93

To assess a possible uncertainty due to the first source, we study efficiencies of tracking and particle identification for charged pions and kaons, as well as π^0 reconstruction, based on doubly tagged $D^0\bar{D}^0$ and D^+D^- samples. We estimate uncertainties while observing how well our MC simulates these efficiencies in data with different particle multiplicities.

We evaluate the effect of the second source for both tracks and π^0s by reweighting the MC to better match the multiplicities in data. In this we assume that data and MC are consistent in the single track and π^0 reconstruction efficiencies. We obtain corrected efficiencies separately for each tag mode, and the difference with the nominal efficiency is used as the systematic uncertainty. The effect is larger for tag modes with greater multiplicity, and so the overall effect on D^+D^- is greater than that on $D^0\bar{D}^0$.

The third source arises due to the fact that we resolve multiple-candidate events when choosing single tags based on the smallest $|\Delta E|$. This selection is imperfect and sometimes the wrong candidate is chosen, lowering the efficiency for multiple-candidate events relative to single-candidate events. Although a best-candidate selection is also applied to double tags, the number of multiple candidates in this case is small and the selection based on two beam-constrained masses is more reliable, so only the systematic uncertainty of best-candidate selection for single tags is considered. Such uncertainty only arises when both the multiple-candidate rate is different between data and MC and the single- and multiple-candidate efficiencies are different. These quantities can be measured both in data and MC, and the observed differences are propagated through to the systematic uncertainties in the cross sections.

Even though we fit both single and double tags to obtain the yields and efficiencies, the differences between one- and two-dimensional fits and the much lower background levels of the double-tag $M_{\rm BC}$ distributions limit the cancellation. We consider several variations of the fitting procedures and use the changes in efficiency-corrected yields to estimate the systematic uncertainties.

The uncertainty due to the single-tag background shape is probed by substituting a MC-derived background for the ARGUS function. The uncertainty due to the signal shape is assessed by altering the smearing of the MC-derived shape (single-Gaussian-convolved instead of the double-Gaussian-convolved). To assess the uncertainty in the double-tag fitting procedure, we obtain double-tag yields and efficiencies with an alternative sideband-subtraction method, dividing the two-dimensional $M_{\rm BC}$ plane into sections representing the signal and various background components, as shown in Fig. 3. The signal area is the same as that used when fitting. Horizontal and vertical bands are used to represent combinations with one correctly and one incorrectly reconstructed D; a diagonal band represents the background from completely reconstructed continuum events or mispartitioned $D\bar{D}$ events; and two triangles are used to represent the remaining background, which is mostly flat. An estimate of the flat background is scaled by the ratios of the sizes of each of the other background regions and subtracted to obtain estimates of the non-flat backgrounds. These backgrounds are then scaled with area and ARGUS background parameters obtained from single-tag fits to determine the overall background subtraction and yield for the signal region for a specific tag mode. The difference in efficiency-corrected double-tag yields for each mode between this method and the standard procedure is taken as the systematic uncertainty associated with the double-tag fitting method.

The cosmic and lepton veto suppresses cosmic ray and QED background in the single-tag selection for the $D^0\to K^-\pi^+$ mode. A cosmic ray background event is produced by a single particle that is incorrectly reconstructed as two oppositely charged tracks. The net momentum of the two tracks is therefore close to zero, and typical QED events also have small net momentum. This small momentum produces $M_{\rm BC}$ values close to the beam energy, so that residual cosmic ray and QED events passing the veto distort the $M_{\rm BC}$ distribution. Because the processes responsible are not included in our MC samples

or well described by the ARGUS background function, the fit results may be affected. To assess this effect, we performed alternative single-tag fits for $D^0\to K^-\pi^+$ with a cut-off in $M_{\rm BC}$ at 1.88 GeV/c^2, excluding the range where cosmic and QED events can contribute. We found the resulting difference from the standard fit procedure to be 0.18%, which we take as the systematic uncertainty due to this effect.

The line shape of the $\psi(3770)$ affects our analysis through the modeling of initial-state radiation (ISR) at the peak of the resonance. The cross section for $\psi(3770)$ production in radiative events depends on the cross section value at the lower effective $E_{\rm cm}$ that results from ISR. While this may partially cancel in the ratio, we treat it separately for single and double tags because yields and efficiencies are affected with opposite signs, and because correlations are introduced for the double-tag fits that are not present in the single-tag fits. The MC-determined efficiencies are affected through the ΔE requirements, which select against large ISR because the ΔE calculation assumes that the energy available to the D is the full beam energy. The data yields are affected via the $M_{\rm BC}$ fit shape, which acquires an asymmetric high-side tail through the contribution of $\psi(3770)$ production via ISR. More ISR causes a larger high-side tail in both the single- and double-tag signal shapes. Additionally, because both D mesons lose energy when ISR occurs, double-tag events that include ISR will have a correlated shift in $M_{\rm BC}$, causing such events to align with the diagonal to the high-side of the signal region in the two-dimensional $M_{\rm BC}$ plane. We use a preliminary BESIII measurement of the $\psi(3770)$ line shape to re-weight the MC and repeat the D-counting procedure. Combining the mode-by-mode variations in $N_{\rm D\bar{D}}$ leads to the systematic uncertainty associated with the $\psi(3770)$ line shape given in Table 6.

The MC modeling of final-state radiation (FSR) may lead to a systematic difference between data and MC tag-reconstruction efficiencies. FSR affects our measurement from the tag-side, so any systematic effect will also have some cancellation. To assess the uncertainty due to FSR we created signal MC samples with and without modeling of FSR and measured the changes in tag reconstruction efficiencies. The largest difference was for $D^0\to K^-\pi^+$, where the relative change in single-tag reconstruction efficiency was 4%. The $D^0\to K^-\pi^+$,$\bar{D}^0\to K^+\pi^-$ double-tag reconstruction efficiency also changed when FSR was turned off, but the cancellation was not complete, with the ratio of efficiencies changing by 1.2%. Because the variation of turning on and off FSR modeling is judged to be too extreme (FSR definitely happens), we take 25% of this difference as our systematic uncertainty due to FSR modeling, a 0.3% relative uncertainty on the MC reconstruction efficiency ratio. To be conservative, we take the largest change, for the $D^0\to K^-\pi^+$ mode, as the systematic uncertainty for all modes.

The correction in the $D^0\bar{D}^0$ cross section due to the treatment of quantum correlations incurs systematic uncertainty associated with the parameters x, y, $\delta_{K\pi}$, and $r^2_{K\pi}$, for which Ref. [19] provides correlation coefficients. Ref. [20] provides a similar coefficient table for the rest of the variables. In evaluating our systematic uncertainty, we have doubled the reported uncertainties and treated them incoherently. Toy MC calculations were used to propagate these uncertainties to $N_{\rm D^0\bar{D}^0}$, giving a systematic uncertainty in the $D^0\bar{D}^0$ cross section of 0.2%.

Finally, for the calculation of cross sections, the relative systematic uncertainty due to the integrated luminosity measurement is determined in Ref. [7, 8] to be 0.5%.

9 Results and conclusions

The separate sources of systematic uncertainty given in Table 6 are combined, taking correlations among them into account, to give overall systematic uncertainties in the $D^0\bar{D}^0$ and D^+D^- cross sections of 1.05% and 0.93%, respectively. Including these systematic uncertainties, the final results of our analysis are as follows:

$$\begin{aligned} N_{\rm D^0\bar{D}^0} &= (10{,}597\pm28\pm98)\times10^3,\\ N_{\rm D^+D^-} &= (8{,}296\pm31\pm65)\times10^3,\\ \sigma(e^+e^-\to D^0\bar{D}^0) &= (3.615\pm0.010\pm0.038)\ {\rm nb},\\ \sigma(e^+e^-\to D^+D^-) &= (2.830\pm0.011\pm0.026)\ {\rm nb},\\ \sigma(e^+e^-\to D\bar{D}) &= (6.445\pm0.015\pm0.048)\ {\rm nb}, \end{aligned}$$

and

$$\begin{aligned} &\sigma(e^+e^-\to D^+D^-)/\sigma(e^+e^-\to D^0\bar{D}^0)\\ &\quad= (78.29\pm0.36\pm0.93)\%, \end{aligned}$$

where the uncertainties are statistical and systematic, respectively. In the determinations of $\sigma(e^+e^-\to D\bar{D})$ and $\sigma(e^+e^-\to D^+D^-)/\sigma(e^+e^-\to D^0\bar{D}^0)$, the uncertainties of the charged and neutral cross sections are mostly uncorrelated, except the systematic uncertainties due to the assumed $\psi(3770)$ line shape, the FSR simulation, and the measurement of the integrated luminosity.

In conclusion, we have used 2.93 fb^{-1} of e^+e^- annihilation data at the $\psi(3770)$ resonance collected by the BESIII detector at the BEPCII collider to measure the cross sections for the production of $D^0\bar{D}^0$ and D^+D^-. The technique is full reconstruction of three D^0 and six D^+ hadronic decay modes and determination of the number of $D^0\bar{D}^0$ and D^+D^- events using the ratio of single-tag and double-tag yields. We find the cross sections to be $\sigma(e^+e^-\to D^0\bar{D}^0) = (3.615\pm0.010\pm0.038)$ nb and $\sigma(e^+e^-\to D^+D^-) = (2.830\pm0.011\pm0.026)$ nb, where the uncertainties are statistical and systematic, respectively. These results are consistent with and more precise than

the previous best measurement by the CLEO-c Collaboration [4] and are necessary input for normalizing some measurements of charmed meson properties in $\psi(3770)$ decays.

The authors are grateful to Werner Sun of Cornell University for very helpful discussions. The BESIII collaboration thanks the staff of BEPCII and the computing center for their hard efforts.

Appendix A

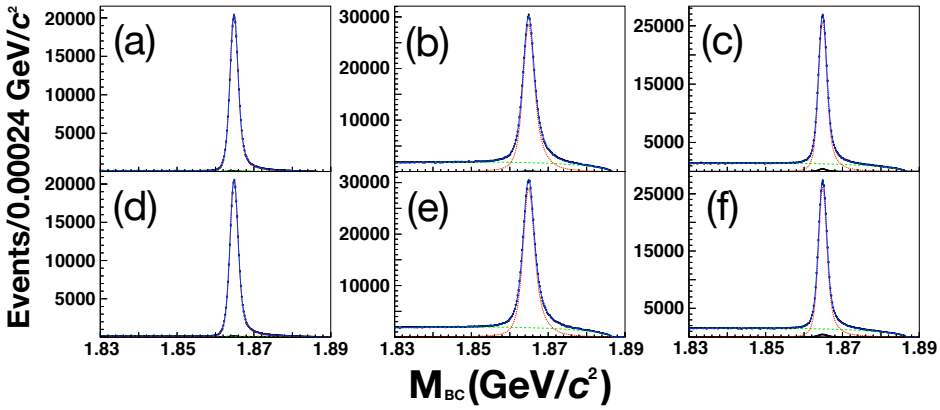

Fig. A1. (color online) $M_{\rm BC}$ fits for single-tag modes; (a) $D^0\to K^-\pi^+$, (b) $D^0\to K^-\pi^+\pi^0$, (c) $D^0\to K^-\pi^+\pi^+\pi^-$, (d) $\bar{D}^0\to K^+\pi^-$, (e) $\bar{D}^0\to K^+\pi^+\pi^-\pi^-$, (f) $\bar{D}^0\to K^+\pi^+\pi^-\pi^-$. Blue solid, red dotted, and green dashed lines represent the total fits, the fitted signal shapes, and the fitted background shapes, respectively, while black histograms correspond to the expected peaking background components.

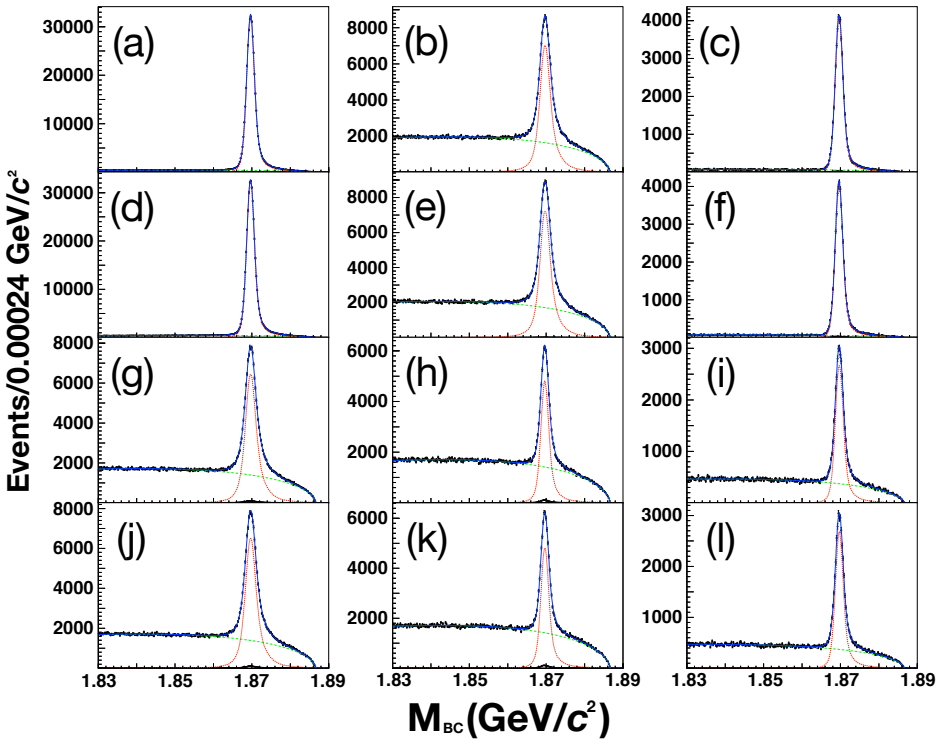

Fig. A2. (color online) $M_{\rm BC}$ fits for single-tag modes; (a) $D^+\to K^-\pi^+\pi^+$, (b) $D^+\to K^-\pi^+\pi^+\pi^0$, (c) $D^+\to K^0_S\pi^+$, (d) $D^-\to K^+\pi^-\pi^-$, (e) $D^-\to K^+\pi^-\pi^-\pi^0$, (f) $D^-\to K^0_S\pi^-$, (g) $D^+\to K^0_S\pi^+\pi^0$, (h) $D^+\to K^0_S\pi^+\pi^+\pi^-$, (i) $D^+\to K^+K^-\pi^+$, (j) $D^-\to K^0_S\pi^-\pi^0$, (k) $D^-\to K^0_S\pi^+\pi^-\pi^-$, (l) $D^-\to K^+K^-\pi^-$. Blue solid, red dotted, and green dashed lines represent the total fits, the fitted signal shapes, and the fitted background shapes, respectively, while black histograms correspond to the expected peaking background components.

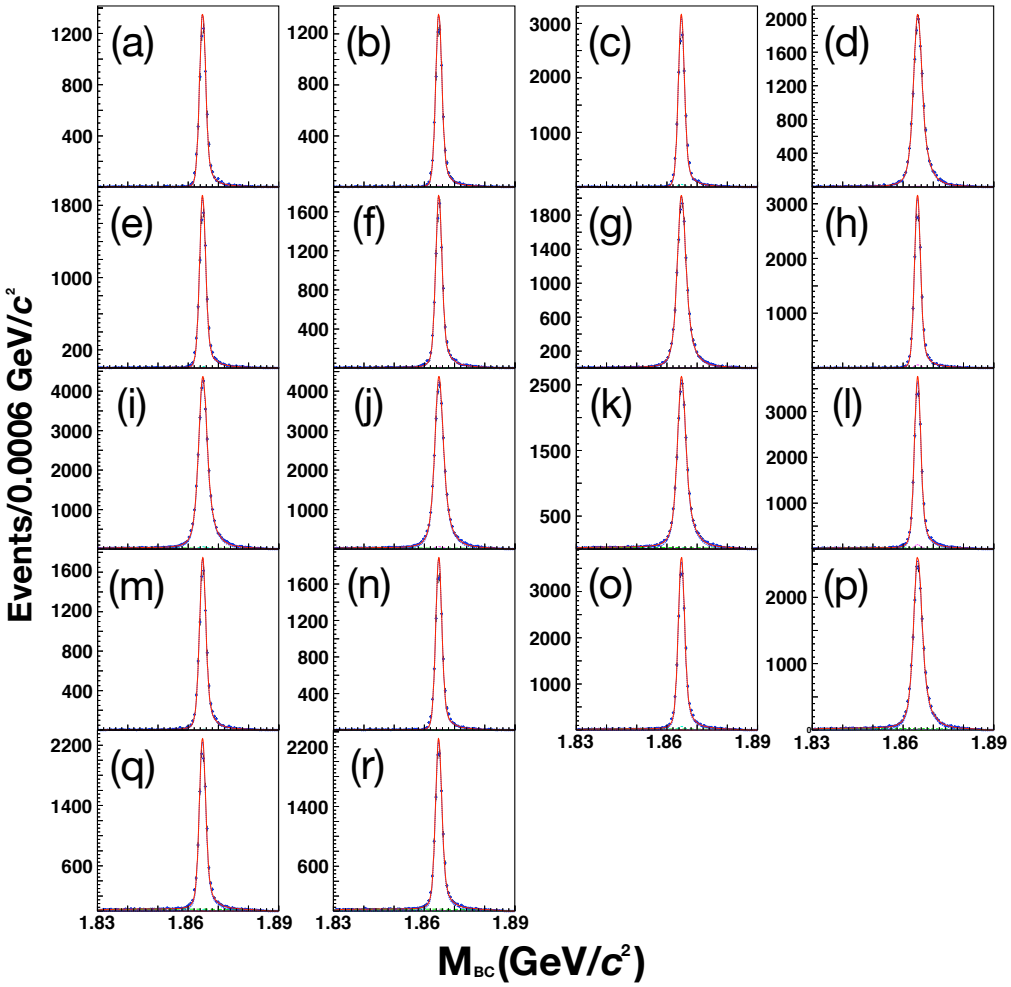

Fig. A3. (color online) Two-dimensional $M_{\rm BC}$ fits projected onto the positive and negative charm $M_{\rm BC}$ axes for various double-tag modes; (a) $D^0 \to K^-\pi^+$ vs. (b) $\bar{D}^0 \to K^+\pi^-$, (c) $D^0 \to K^-\pi^+$ vs. (d) $\bar{D}^0 \to K^+\pi^-\pi^0$, (e) $D^0 \to K^-\pi^+$ vs. (f) $\bar{D}^0 \to K^+\pi^+\pi^-\pi^-$, (g) $D^0 \to K^-\pi^+\pi^0$ vs. (h) $\bar{D}^0 \to K^+\pi^-$, (i) $D^0 \to K^-\pi^+\pi^0$ vs. (j) $\bar{D}^0 \to K^+\pi^-\pi^0$, (k) $D^0 \to K^-\pi^+\pi^0$ vs. (l) $\bar{D}^0 \to K^+\pi^+\pi^-\pi^-$, (m) $D^0 \to K^-\pi^+\pi^+\pi^-$ vs. (n) $\bar{D}^0 \to K^+\pi^-$, (o) $D^0 \to K^-\pi^+\pi^+\pi^-$ vs. (p) $\bar{D}^0 \to K^+\pi^-\pi^0$, (q) $D^0 \to K^-\pi^+\pi^+\pi^-$ vs. (r) $\bar{D}^0 \to K^+\pi^+\pi^-\pi^-$. Red solid and blue dotted curves represent the total fits and the fitted signal shapes, respectively. Green long-dashed and orange solid lines correspond to the fitted non-peaking background shapes, while cyan and magenta short-dashed curves are the fitted peaking background components.

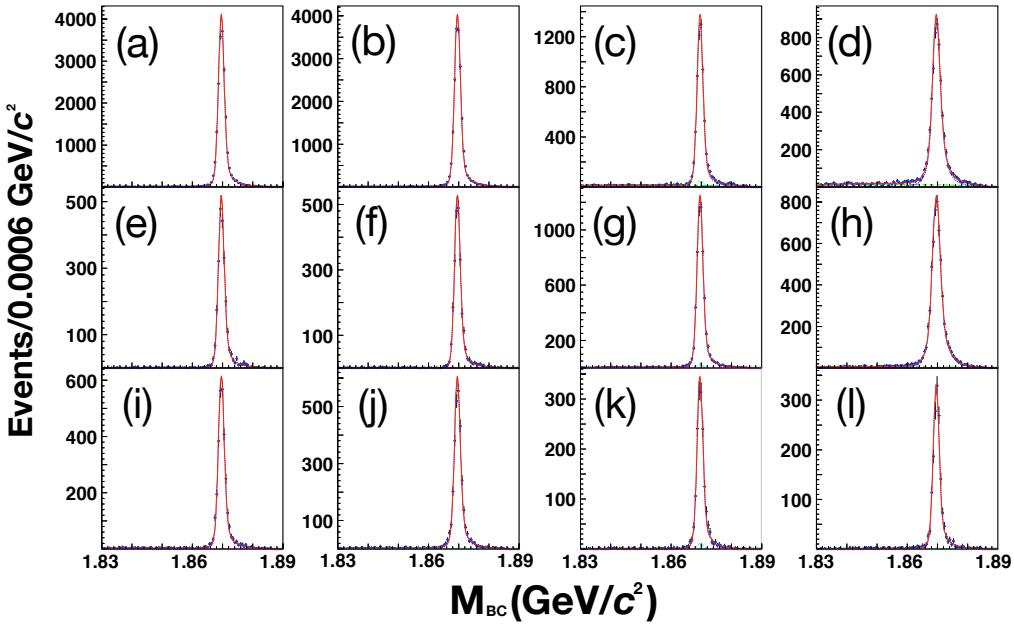

Fig. A4. (color online) Two-dimensional $M_{\rm BC}$ fits projected onto the positive and negative charm $M_{\rm BC}$ axes for various double-tag modes; (a) $D^+\to K^-\pi^+\pi^+$ vs. (b) $D^-\to K^+\pi^-\pi^-$, (c) $D^+\to K^-\pi^+\pi^+$ vs. (d) $D^-\to K^+\pi^-\pi^-\pi^0$, (e) $D^+\to K^-\pi^+\pi^+$ vs. (f) $D^-\to K^0_S\pi^-$, (g) $D^+\to K^-\pi^+\pi^+$ vs. (h) $D^-\to K^0_S\pi^-\pi^0$, (i) $D^+\to K^-\pi^+\pi^+$ vs. (j) $D^-\to K^0_S\pi^+\pi^-\pi^-$, (k) $D^+\to K^-\pi^+\pi^+$ vs. (l) $D^-\to K^+K^-\pi^-$. Red solid and blue dotted curves represent the total fits and the fitted signal shapes, respectively. Green long-dashed and orange solid lines correspond to the fitted non-peaking background shapes, while cyan and magenta short-dashed curves are the fitted peaking background components.

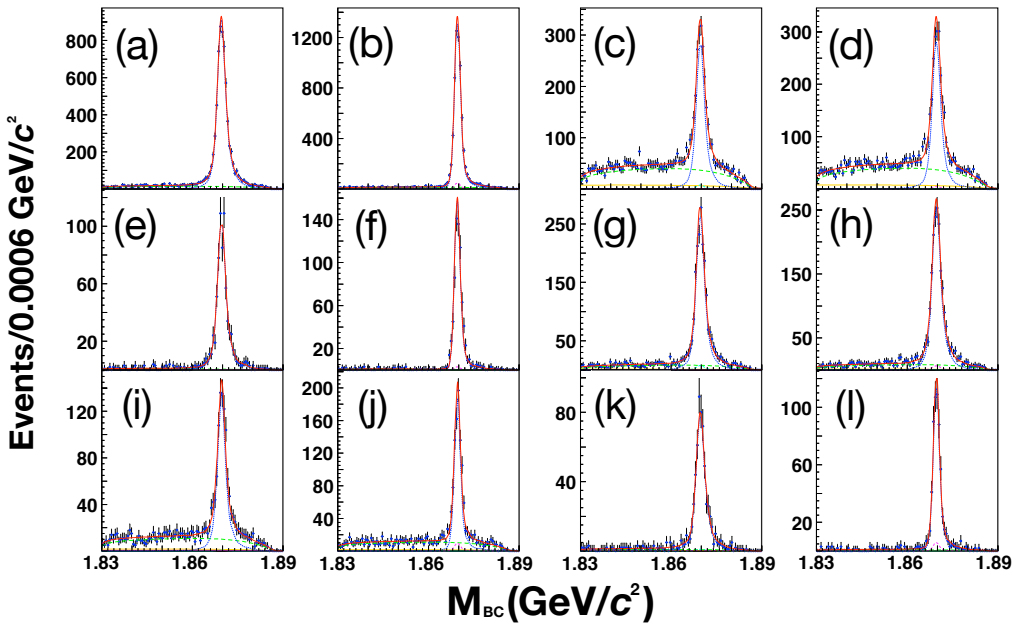

Fig. A5. (color online) Two-dimensional $M_{\rm BC}$ fits projected onto the positive and negative charm $M_{\rm BC}$ axes for various double-tag modes; (a) $D^+\to K^-\pi^+\pi^+\pi^0$ vs. (b) $D^-\to K^+\pi^-\pi^-$, (c) $D^+\to K^-\pi^+\pi^+\pi^0$ vs. (d) $D^-\to K^+\pi^-\pi^-\pi^0$, (e) $D^+\to K^-\pi^+\pi^+\pi^0$ vs. (f) $D^-\to K^0_S\pi^-$, (g) $D^+\to K^-\pi^+\pi^+\pi^0$ vs. (h) $D^-\to K^0_S\pi^-\pi^0$, (i) $D^+\to K^-\pi^+\pi^+\pi^0$ vs. (j) $D^-\to K^0_S\pi^+\pi^-\pi^-$, (k) $D^+\to K^-\pi^+\pi^+\pi^0$ vs. (l) $D^-\to K^+K^-\pi^-$. Red solid and blue dotted curves represent the total fits and the fitted signal shapes, respectively. Green long-dashed and orange solid lines correspond to the fitted non-peaking background shapes, while cyan and magenta short-dashed curves are the fitted peaking background components.

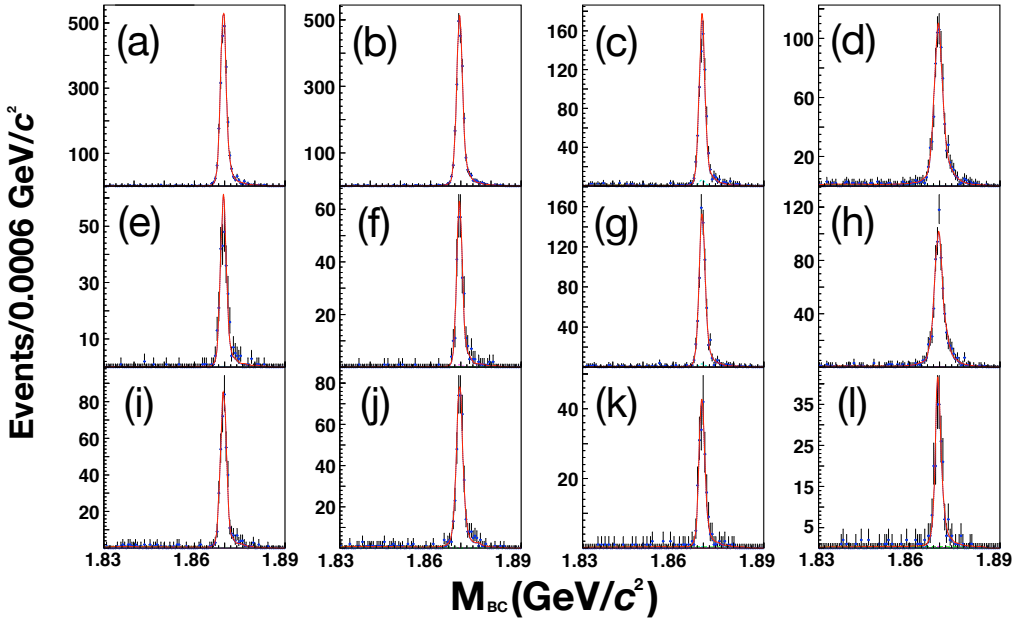

Fig. A6. (color online) Two-dimensional $M_{\rm BC}$ fits projected onto the positive and negative charm $M_{\rm BC}$ axes for various double-tag modes; (a) $D^+\to K^0_S\pi^+$ vs. (b) $D^-\to K^+\pi^-\pi^-$, (c) $D^+\to K^0_S\pi^+$ vs. (d) $D^-\to K^+\pi^-\pi^-\pi^0$, (e) $D^+\to K^0_S\pi^+$ vs. (f) $D^-\to K^0_S\pi^-$, (g) $D^+\to K^0_S\pi^+$ vs. (h) $D^-\to K^0_S\pi^-\pi^0$, (i) $D^+\to K^0_S\pi^+$ vs. (j) $D^-\to K^0_S\pi^+\pi^-\pi^-$, (k) $D^+\to K^0_S\pi^+$ vs. (l) $D^-\to K^+K^-\pi^-$. Red solid and blue dotted curves represent the total fits and the fitted signal shapes, respectively. Green long-dashed and orange solid lines correspond to the fitted non-peaking background shapes, while cyan and magenta short-dashed curves are the fitted peaking background components.

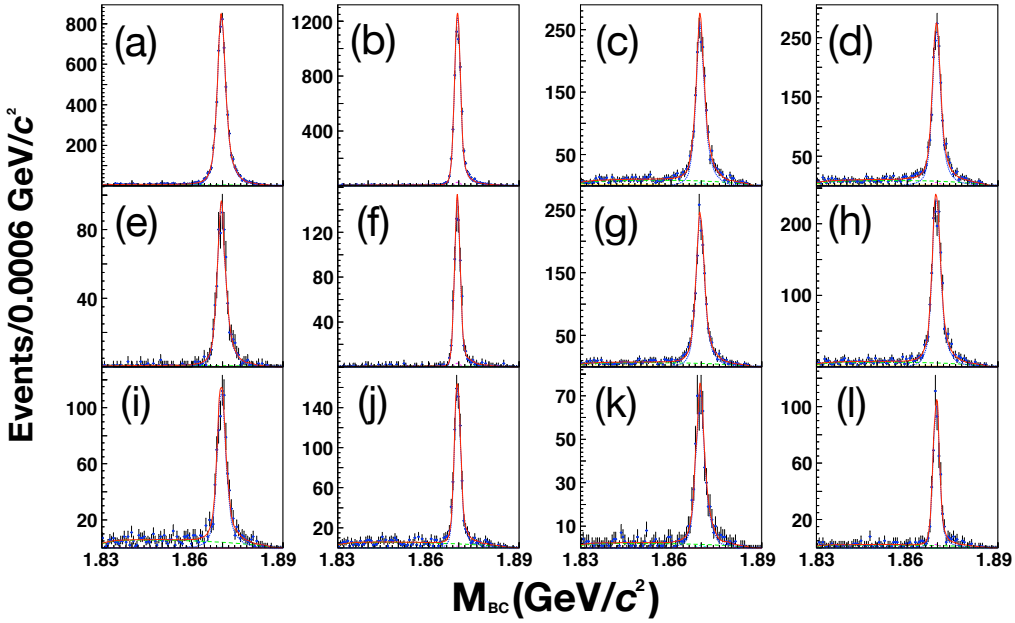

Fig. A7. (color online) Two-dimensional $M_{\rm BC}$ fits projected onto the positive and negative charm $M_{\rm BC}$ axes for various double-tag modes; (a) $D^+\to K^0_S\pi^+\pi^0$ vs. (b) $D^-\to K^+\pi^-\pi^-$, (c) $D^+\to K^0_S\pi^+\pi^0$ vs. (d) $D^-\to K^+\pi^-\pi^-\pi^0$, (e) $D^+\to K^0_S\pi^+\pi^0$ vs. (f) $D^-\to K^0_S\pi^-$, (g) $D^+\to K^0_S\pi^+\pi^0$ vs. (h) $D^-\to K^0_S\pi^-\pi^0$, (i) $D^+\to K^0_S\pi^+\pi^0$ vs. (j) $D^-\to K^0_S\pi^+\pi^-\pi^-$, (k) $D^+\to K^0_S\pi^+\pi^0$ vs. (l) $D^-\to K^+K^-\pi^-$. Red solid and blue dotted curves represent the total fits and the fitted signal shapes, respectively. Green long-dashed and orange solid lines correspond to the fitted non-peaking background shapes, while cyan and magenta short-dashed curves are the fitted peaking background components.

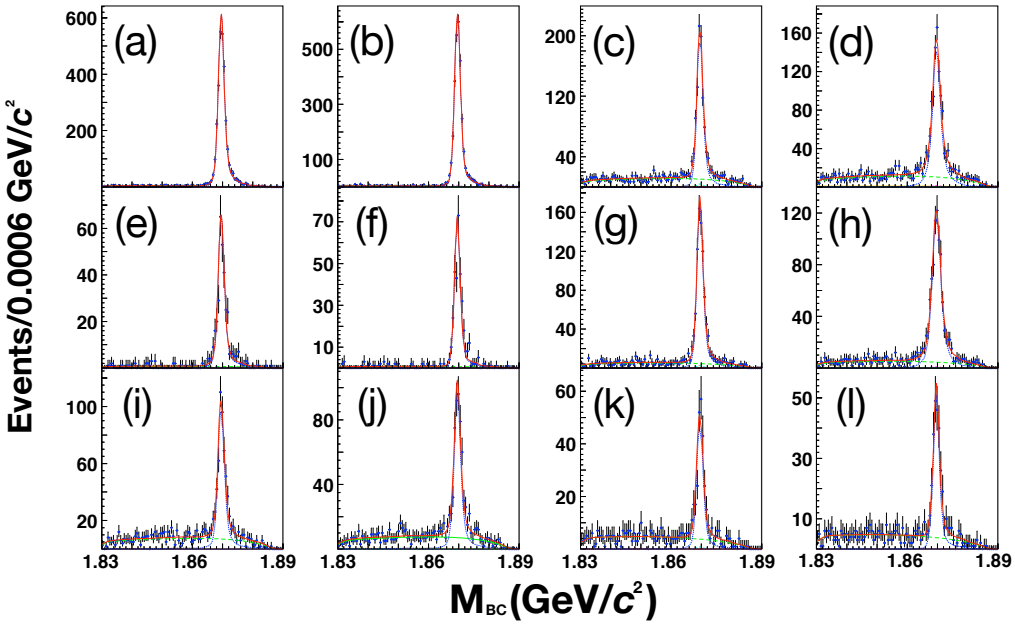

Fig. A8. (color online) Two-dimensional $M_{\rm BC}$ fits projected onto the positive and negative charm $M_{\rm BC}$ axes for various double-tag modes; (a) $D^+\to K^0_S\pi^+\pi^+\pi^-$ vs. (b) $D^-\to K^+\pi^-\pi^-$, (c) $D^+\to K^0_S\pi^+\pi^+\pi^-$ vs. (d) $D^-\to K^+\pi^-\pi^-\pi^0$, (e) $D^+\to K^0_S\pi^+\pi^+\pi^-$ vs. (f) $D^-\to K^0_S\pi^-$, (g) $D^+\to K^0_S\pi^+\pi^+\pi^-$ vs. (h) $D^-\to K^0_S\pi^-\pi^0$, (i) $D^+\to K^0_S\pi^+\pi^+\pi^-$ vs. (j) $D^-\to K^0_S\pi^+\pi^-\pi^-$, (k) $D^+\to K^0_S\pi^+\pi^+\pi^-$ vs. (l) $D^-\to K^+K^-\pi^-$. Red solid and blue dotted curves represent the total fits and the fitted signal shapes, respectively. Green long-dashed and orange solid lines correspond to the fitted non-peaking background shapes, while cyan and magenta short-dashed curves are the fitted peaking background components.

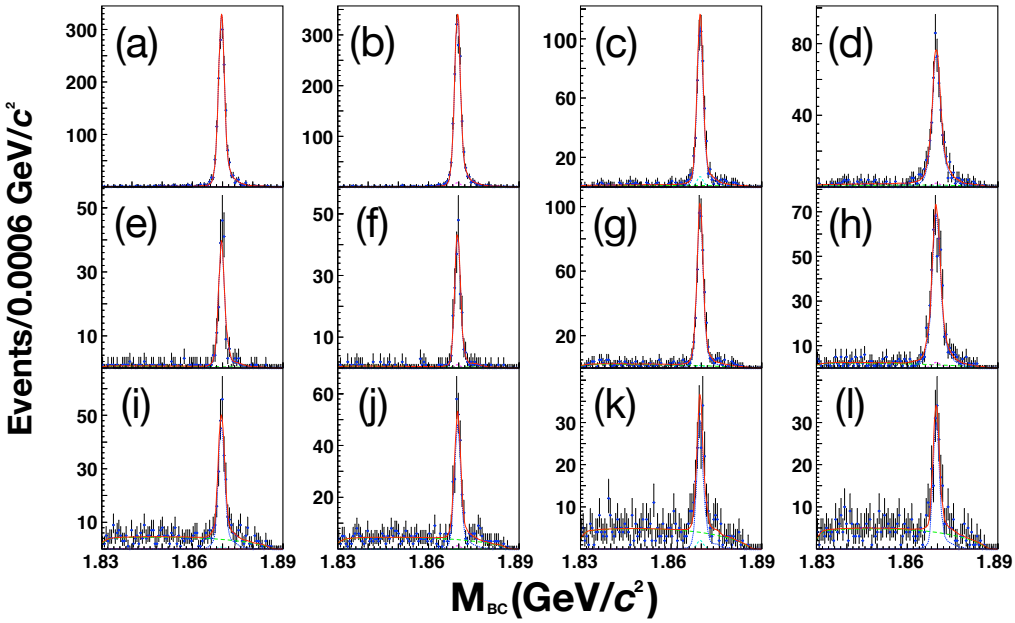

Fig. A9. (color online) Two-dimensional $M_{\rm BC}$ fits projected onto the positive and negative charm $M_{\rm BC}$ axes for various double-tag modes; (a) $D^+\to K^+K^-\pi^+$ vs. (b) $D^-\to K^+\pi^-\pi^-$, (c) $D^+\to K^+K^-\pi^+$ vs. (d) $D^-\to K^+\pi^-\pi^-\pi^0$, (e) $D^+\to K^+K^-\pi^+$ vs. (f) $D^-\to K^0_S\pi^-$, (g) $D^+\to K^+K^-\pi^+$ vs. (h) $D^-\to K^0_S\pi^-\pi^0$, (i) $D^+\to K^+K^-\pi^+$ vs. (j) $D^-\to K^0_S\pi^+\pi^-\pi^-$, (k) $D^+\to K^+K^-\pi^+$ vs. (l) $D^-\to K^+K^-\pi^-$. Red solid and blue dotted curves represent the total fits and the fitted signal shapes, respectively. Green long-dashed and orange solid lines correspond to the fitted non-peaking background shapes, while cyan and magenta short-dashed curves are the fitted peaking background components.

References

1 C. Patrignani et al (Particle Data Group], Chin. Phys. C, **40**: 100001 (2016) Some of the MC simulations were generated with inputs taken from earlier editions of the PDG review
2 M. Ablikim et al (BES Collaboration), Phys. Lett. B, **659**: 74 (2008)
3 D. Besson et al (CLEO Collaboration), Phys. Rev. Lett., **96**: 092002 (2006); Phys. Rev. Lett., **104**: 159901 (2010)
4 G. Bonvicini et al (CLEO Collaboration), Phys. Rev. D, **89**: 072002 (2014); Phys. Rev. D, **91**: 019903 (2015)
5 R. M. Baltrusaitis et al (MARK-III Collaboration), Phys. Rev. Lett., **56**: 2140 (1986)
6 D. M. Asner and W. M. Sun, Phys. Rev. D, **73**: 034024 (2006); Phys. Rev. D, **77**: 019901 (2008)
7 M. Ablikim et al (BESIII Collaboration), Chin. Phys. C, **37**: 123001 (2013)
8 M. Ablikim et al (BESIII Collaboration), Phys. Lett. B, **753**: 629 (2016); G. Balossini et al, Nucl. Phys. B, **758**: 227 (2006); S. Actis et al (Working Group on Radiative Corrections and Monte Carlo Generators for Low Energies), Eur. Phys. J. C, **66**: 585 (2010)
9 M. Ablikim et al (BESIII Collaboration), Nucl. Instrum. Meth. A, **614**: 345 (2010)
10 S. Agostinelli et al (GEANT4 Collaboration), Nucl. Instrum. Meth. A, **506**: 250 (2003)
11 S. Jadach, B. F. L. Ward, and Z. Was, Comput. Phys. Commun., **130**: 260 (2000)
12 S. Jadach, B. F. L. Ward, and Z. Was, Phys. Rev. D, **63**: 113009 (2001)
13 D. J. Lange, Nucl. Instrum. Meth. A, **462**: 152 (2001); R. G. Ping, Chin. Phys. C **32**, 599 (2008)
14 J. C. Chen, G. S. Huang, X. R. Qi, D. H. Zhang, and Y. S. Zhu, Phys. Rev. D,**62**: 034003 (2000)
15 S. Jadach, J. H. Kühn, and Z. Was, Comput. Phys. Commun., **64**: 275 (1990); M. Jezabek, Z. Was, S. Jadach, and J. H. Kühn, Comput. Phys. Commun., **70**: 69 (1992); S. Jadach, Z. Was, R. Decker, and J. H. Kühn, Comput. Phys. Commun., **76**: 361 (1993); P. Golonka et al, Comput. Phys. Commun., **174**: 818 (2006)
16 M. Ablikim et al (BESIII Collaboration), Phys. Lett. B, **744**: 339 (2015)
17 H. Albrecht et al (ARGUS Collaboration), Phys. Lett. B, **241**: 278 (1990)
18 D. M. Asner et al (CLEO Collaboration), Phys. Rev. D, **86**: 112001 (2012)
19 Heavy Flavor Averaging Group (HFLAV), (http://www.slac.stanford.edu/xorg/hflav/charm/).
20 T. Evans et al, Phys. Lett. B, **757**: 520 (2016)